

# Journal of Geophysical Research: Solid Earth

## RESEARCH ARTICLE

10.1002/2015JB012621

**Key Points:**

- Seismicity and crustal structure elucidates the mode of deformation in the rifting Papuan crust
- Extension not diapirism drives core complex exhumation
- Intermediate-depth earthquakes are discovered, related to young ultra-high-pressure metamorphism

**Supporting Information:**

- Figures S1–S3

**Correspondence to:**G. A. Abers,  
abers@cornell.edu**Citation:**

Abers, G. A., Z. Eilon, J. B. Gaherty, G. Jin, YH. Kim, M. Obrebski, and C. Dieck (2016), Southeast Papuan crustal tectonics: Imaging extension and buoyancy of an active rift, *J. Geophys. Res. Solid Earth*, 121, 951–971, doi:10.1002/2015JB012621.

Received 25 OCT 2015

Accepted 19 JAN 2016

Accepted article online 22 JAN 2016

Published online 19 FEB 2016

## Southeast Papuan crustal tectonics: Imaging extension and buoyancy of an active rift

**G. A. Abers<sup>1</sup>, Z. Eilon<sup>2,3</sup>, J. B. Gaherty<sup>2</sup>, G. Jin<sup>3,4</sup>, YH. Kim<sup>5</sup>, M. Obrebski<sup>2,6</sup>, and C. Dieck<sup>2,7</sup>**

<sup>1</sup>Department of Earth and Atmospheric Sciences, Cornell University, Ithaca, New York, USA, <sup>2</sup>Lamont-Doherty Earth Observatory of Columbia University, Palisades, New York, USA, <sup>3</sup>Department of Earth and Environmental Sciences, Columbia University, New York, New York, USA, <sup>4</sup>Now at ConocoPhillips, Houston, Texas, USA, <sup>5</sup>School of Earth and Environmental Sciences, Seoul National University, Seoul, South Korea, <sup>6</sup>Now at ESIGELEC Graduate School of Engineering, Saint-Etienne du Rouvray, France, <sup>7</sup>Now at Gemological Institute of America, New York, New York, USA

**Abstract** Southeast Papua hosts the world's youngest ultra-high-pressure (UHP) metamorphic rocks. These rocks are found in an extensional setting in metamorphic core complexes. Competing theories of extensional shear zones or diapiric upwelling have been suggested as driving their exhumation. To test these theories, we analyze the CDPAPUA temporary array of 31 land and 8 seafloor broadband seismographs. Seismicity shows that deformation is being actively accommodated on the core complex bounding faults, offset by transfer structures in a manner consistent with overall north-south extension rather than radial deformation. Rayleigh wave dispersion curves are jointly inverted with receiver functions for crustal velocity structure. They show crustal thinning beneath the core complexes of 30–50% and very low shear velocities at all depths beneath the core complexes. On the rift flanks velocities resemble those of normal continents and increase steadily with depth. There is no evidence for velocity inversions that would indicate that a major density inversion exists to drive crustal diapirs. Also, low-density melt seems minor within the crust. Together with the extension patterns apparent in seismicity, these data favor an extensional origin for the core complexes and limit the role of diapirism as a secondary exhumation mechanism, although deeper mantle diapirs may be undetected. A small number of intermediate-depth earthquakes, up to 120 km deep, are identified for the first time just northeast of the D'Entrecasteaux Islands. They occur at depths similar to those recorded by UHP rocks and similar temperatures, indicating that the modern seismicity occurs at the setting that generates UHP metamorphism.

### 1. Introduction

Metamorphic rocks frequently occur in domal structures ringed by low-grade rocks, termed gneiss domes or metamorphic core complexes, in many extensional settings [e.g., Coney, 1980; Whitney et al., 2013]. Their exhumation has been variably attributed to extensional unroofing [Davis and Lister, 1988] or buoyant diapirism [Teyssier and Whitney, 2002], but it is unclear in many cases which mechanism dominates. We address this question at a rare example of active dome exhumation at the D'Entrecasteaux-Woodlark domes of Papua New Guinea (Figure 1). This rift includes three gneissic domes on Fergusson and Goodenough Islands of the D'Entrecasteaux Islands, the Dayman Dome on the Papuan Peninsula of New Guinea, and overprinted examples farther east. The D'Entrecasteaux domes are frequently described as metamorphic core complexes or MCCs [e.g., Davies and Warren, 1988; Hill et al., 1992], so for convenience we will refer to these structures as such.

Extension clearly plays a role in unroofing at some stage. Exhumation of high-grade rocks from middle to lower crustal [Hill et al., 1992] and upper mantle depths [Baldwin et al., 2008; Gordon et al., 2012] is synchronous with extension over the last 4–8 Ma [e.g., Taylor and Huchon, 2002]. The structure of the shear zone and related brittle features indicates crustal-scale north dipping detachment faults [Davies and Warren, 1988], a view supported by subsequent mapping [e.g., Hill et al., 1992] and earthquake studies [Abers, 1991; Abers et al., 1997], although radial fabrics on the bounding shear zones indicate a more complicated exhumation scenario [Little et al., 2011]. The discovery of high-pressure and ultra-high-pressure (UHP) metamorphic rocks [Baldwin et al., 2004, 2008] has motivated models of earlier subduction followed by wholesale reversal [Webb et al., 2008] and eduction or buoyancy-driven reversal of subduction [Petersen and Buck, 2015]. In both cases, footwall rocks are exhumed along modestly dipping detachments.

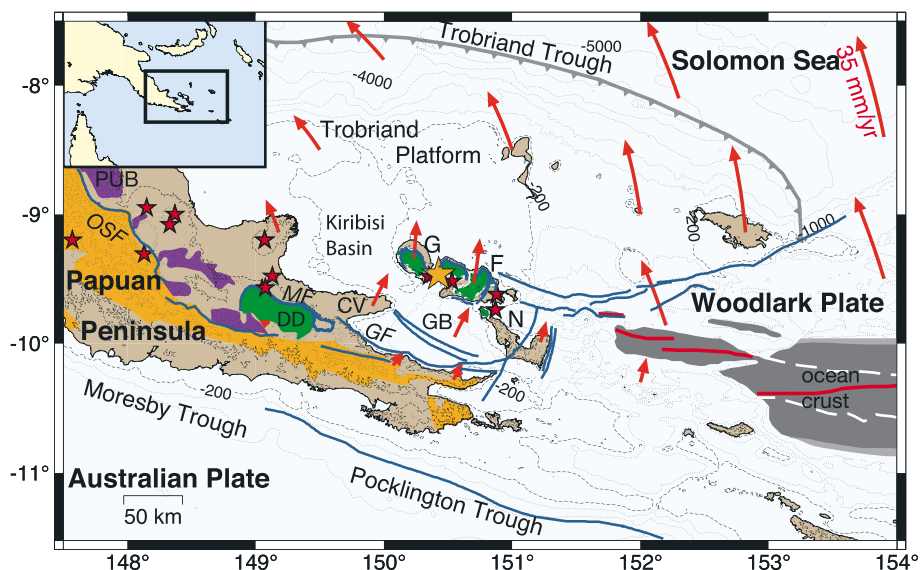


**Figure 1.** Main tectonic features of the Woodlark-D'Entrecasteaux Rift. Blue lines show selected active faults, and toothed gray line shows inactive Trobriand Trough. Purple field shows ultramafic rocks, orange shows Owen Stanley Metamorphics, and green shows main MCCs [e.g., Baldwin et al., 2008; Little et al., 2011]. Gray field shows new oceanic crust, and red line at center is spreading axis [Taylor et al., 1999]. Red stars show Quaternary volcanic centers [Smith and Milsom, 1984]; orange star shows UHP locality [Baldwin et al., 2008]; red arrows show GPS model velocities relative to Australia [Wallace et al., 2014]. Labeled features include the D'Entrecasteaux Islands, G: Goodenough Island, F: Fergusson Island, and N: Normanby. Other abbreviations are PUB: southeast end of Papuan Ultramafic Belt, OSF: Owen Stanley Fault, DD: Dayman Dome, MF: Mai'u Fault, CV: Cape Vogel, GF: Goodenough Bay Fault, and GB: Goodenough Basin. Dashed line shows 200 m water depth; dotted lines contour deeper depths at 1000 m intervals.

However, several authors have argued that the MCCs represent buoyant diapirs, driven by either crustal density inversions resulting from shallow ophiolite emplacement [Martinez et al., 2001] or mantle buoyancy of subducted continental crust [Ellis et al., 2011]. Evidence for diapirism includes radial patterns of lineations around individual domes [Little et al., 2011] and an apparent lack of significant extension in basins along strike west of the D'Entrecasteaux domes [Fitz and Mann, 2013]. Although such diapirism may be happening concurrent with extension, in many interpretations they cut through the hanging wall and so are fundamentally driven by buoyancy not extension.

This paper presents new results from a broadband seismic array deployed in the region in 2010–2011 [Eilon et al., 2014, 2015; Jin et al., 2015]. Seismicity recorded by this array clearly illustrates many of the active fault systems in the region and shows that the faults bounding the D'Entrecasteaux MCCs are active along their entire length. The D'Entrecasteaux MCCs step southward to similar faults on the Papuan Peninsula along a transfer fault system akin to continental transforms and show that exhumation and extension are tightly linked. Joint inversion of receiver functions and surface-wave dispersion confirms 30–50% thinner crust and low crustal velocities along the D'Entrecasteaux MCC axis, surrounded by thicker continental crust. The seismic velocities in the surrounding crust are inconsistent with many aspects of models that unroof MCCs by diapirism. Overall, these data show the essentially extensional nature of the D'Entrecasteaux MCCs and indicate the importance of studying active systems to establish the origin of such features.

## 2. Tectonics of the Rift

Along its strike the Woodlark-D'Entrecasteaux Rift displays the complete sequence of continental breakup from extended crust to seafloor spreading, with the transition near 152°E (Figure 1) [Little et al., 2011; Baldwin et al., 2012; Fitz and Mann, 2013]. Symmetric magnetic anomalies are clearly mapped back to 3.6 Ma, placing a minimum age for the onset of extension throughout the region, and older anomalies on one side of the rift near the Solomon trench indicate some seafloor spreading since 6 Ma [Taylor et al., 1999]. A regional unconformity at 8.4 Ma may date the onset of extension throughout the Trobriand Platform [Taylor and Huchon, 2002]; however, high extension rates are only well documented since 3.6 Ma

[Petersen and Buck, 2015]. The post-3.6 Ma extension takes place about a pole near 147–148°E [e.g., Weissel et al., 1982; Taylor and Huchon, 2002] at 15–35 mm/yr at the longitudes of the MCCs and faster to the east [Taylor et al., 1999]. At 0.52 Ma a change in seafloor fabric indicates a change in the pole and decrease in the rate of opening [Goodliffe et al., 1997]. Geodetic estimates of extension are 20–40% slower than the pre-0.52 Ma magnetic anomalies, probably distributed over multiple faults [Wallace et al., 2004, 2014].

## 2.1. Crustal Composition and Structure

The Papuan Peninsula is a collisional assembly of Cenozoic terranes of noncontinental origin [Pigram and Davies, 1987]. The oldest event to affect the Papuan Peninsula was rifting of the Coral Sea at the margin of Australia at 62–56 Ma [Weissel and Watts, 1979], although the rift flank on the Papuan side cannot be found in outcrop. At 58 Ma the Papuan Ultramafic Belt (PUB) was thrust over the Owen Stanley Metamorphics that make up much of the spine of the Papuan Peninsula [Davies and Jaques, 1984; Lus et al., 2004]. The PUB consists of 4–8 km of ultramafic rocks overlain by 8 km of gabbro and basalt, thought to represent a large obducted slab of oceanic lithosphere related to a Paleocene island arc exposed on Cape Vogel [Davies, 1971]. The coherent ophiolitic sequence, emplaced on the 10–30° northeast dipping Owen Stanley Fault, outcrops west of 148°E and north of 9°S, and gravity modeling and seismic refraction indicate that this 15–20 km thick dipping sequence continues northeastward offshore [Finlayson et al., 1977]. The rocks forming the PUB have been dated at late Maastrichtian (71–65 Ma), and similar age basalts are found throughout the Papuan Peninsula and drilled basement samples of the Trobriand Platform [e.g., Taylor and Huchon, 2002]. Some authors have inferred that the PUB forms the upper crust throughout the D'Entrecasteaux region such that the upper crust is significantly denser than the lower crust [Martinez et al., 2001; Fitz and Mann, 2013]. However, gravity anomalies do not support continuation of a high-density PUB east of 148–149°E [Lindley, 2014] nor do seismic velocities inferred from local earthquake tomography [Ferris et al., 2006]. Most of the basalts east of 149°E have trace elements indicating oceanic plateau rather than arc affinity [Brooks and Tegner, 2001], and the scattered ultramafics may be thin fragments [Baldwin et al., 2012].

At ages between the Paleocene PUB obduction event and the onset of rifting at 3.6–8.4 Ma, scattered Miocene volcanics of island arc affinity were emplaced throughout the region [Smith and Milsom, 1984] and are interpreted as a remnant of the Miocene Maramuni Arc [Baldwin et al., 2012]. The Trobriand Trough has been suggested as the site of south dipping subduction during the Miocene and, arguably, more recently [Davies et al., 1987]. Limited volcanism continues today, with active volcanoes varying from andesitic arc-related stratovolcanoes in the Papuan Peninsula to more bimodal and rift-related centers in the D'Entrecasteaux Islands [Smith and Milsom, 1984].

The D'Entrecasteaux MCCs formed during the late Cenozoic extension, as indicated by young metamorphic ages and an early Pliocene age for the first appearance of metamorphic clasts in adjacent basins [Davies and Warren, 1988]. High-grade metamorphic rocks of the MCCs include 2 Ma midcrustal granites and 2–4 Ma gneisses from middle to lower crustal depths (0.7–1.1 GPa), found in various localities on Goodenough and Fergusson Islands, all indicating temperatures of 550–730°C at these depths [e.g., Baldwin et al., 1993, 2004]. The bulk of the exposed rock on the footwall of the MCCs is felsic in composition. Coesite-bearing eclogites have been found at one location on Fergusson Island (Figure 1) indicating depths in excess of 100 km and temperatures of 600–760°C and dated variably at 5–8 Ma [Baldwin et al., 2008; Gordon et al., 2012]. The Dayman Dome on the Papuan Peninsula also exhumes metamorphic rock on the footwall of a north dipping normal fault, but it lies closer to the pole of opening and exposes lower grade metamorphic rocks [Daczko et al., 2009].

## 2.2. Deeper Structure

A previous earthquake seismic experiment, termed WOODSEIS, shows generally low crustal velocities beneath the eastern D'Entrecasteaux Islands consistent with felsic bulk compositions, grading to higher gabbroic velocities near the oceanic rift tip [Ferris et al., 2006]. Crust also thins beneath the D'Entrecasteaux, reaching only 20–25 km in some places compared with 35 km beneath the Papuan Peninsula [Abers et al., 2002]. This thin crust corresponds to higher rather than lower elevations and is isostatically balanced by a low-density, low-velocity upper mantle [Abers et al., 2002]. The axis of this low-velocity mantle continues without break from the oceanic rift tip westward beneath the MCCs. It is bound sharply to the north by a high-velocity low-temperature mantle structure at depths less than 100 km beneath the Trobriand Platform [Eilon et al., 2015; Jin et al., 2015]. The mantle shows anisotropic mantle fabrics similar to a mid-ocean ridge with spreading-parallel fast directions

[Eilon *et al.*, 2014]; anisotropic body wave tomography shows that the spreading-parallel fast directions lie within hot, asthenospheric mantle (Z. Eilon *et al.*, A joint inversion for shear velocity and anisotropy: The Woodlark Rift, Papua New Guinea, submitted to *Geophysical Journal International*, 2015). Overall, the mantle structure resembles that of an oceanic spreading system being initiated, while the overlying crust still retains many aspects of its quasi-continental origin.

### 2.3. Present-Day Tectonics

East of about 151.7°E, extension is accommodated by seafloor spreading with minor faulting on the northern ridge flank [e.g., Abers *et al.*, 1997; Taylor *et al.*, 1999]. West of Cape Vogel (149.9°E) there is good evidence that extension is being localized along the Mai’iu Fault, a north dipping normal fault and exhumed surface bounding the Suckling-Dayman Dome (Figure 1). Evidence for rapid extension on the Mai’iu Fault includes normal-faulting focal mechanisms of large earthquakes [Abers *et al.*, 1997], geomorphic evidence for exhumation of a nearly uneroded fault surface [Ollier and Pain, 1980; Daczko *et al.*, 2009; Miller *et al.*, 2012], and extensional GPS velocities of 7–9 mm/yr [Wallace *et al.*, 2014].

Between Cape Vogel and the oceanic rift tip the pattern of deformation is less clear. Extension has been inferred both on faults bounding the D’Entrecasteaux Islands MCCs and on the Goodenough Bay Fault bounding the northern Papuan Peninsula. The balance between these two systems reflects the extent to which the MCCs continue to be active extensional structures. GPS surveys indicate a roughly equal division of the 15–20 mm/yr extension between faults north of the D’Entrecasteaux Islands and faults between them and coastal sites, usually assumed to be the Goodenough Bay Fault [Wallace *et al.*, 2014]. Steep stream profiles [Miller *et al.*, 2012] and relatively planar exhumed shear zones [Davies and Warren, 1988] along 30–40° north dipping faults cutting alluvium [Little *et al.*, 2011] attest to relatively young exhumation of the MCCs, as do 0.4–1.0 Ma apatite fission track ages [Baldwin *et al.*, 1993]. Geomorphic evidence indicates that south dipping faults on the south flanks of Goodenough and Fergusson may be active as well [Little *et al.*, 2011; Miller *et al.*, 2012].

A lack of uplifted coral terraces around Goodenough Island and the absence of faults imaged in the Kiribisi Basin immediately west of Goodenough Island have been taken as evidence that MCC-bounding faults do not presently accommodate extension but may be better described as diapirs ascending through unextended crust [Fitz and Mann, 2013]. Little *et al.* [2011] argue that radial lineation patterns on the MCCs favor lateral flow and indicate that the MCCs represent Rayleigh-Taylor diapirs, although related models rely upon extension to accommodate diapiric ascent [Ellis *et al.*, 2011].

## 3. Data

A regional broadband array termed CDPAPUA was deployed from early 2010 to mid-2011 around southeastern Papua, the D’Entrecasteaux Islands, and the Trobriand Platform (Figure 2 and supporting information Figure S1). The array included 31 onshore broadband seismographs, occasionally redeployed for security or noise purposes, and 8 ocean bottom seismographs (OBSs). Onshore instruments had Guralp CMG3-T (120 s period) sensors and digitized continuously at 50 samples per second. The OBSs were from the Scripps OBS Instrument Pool center, with Nanometrics Trillium 240 s broadband sensors and a differential pressure gauge all recorded at 50 sps. All OBS data are time corrected prior to use, and horizontal components were oriented using surface-wave polarizations. Further details about the array can be found in Eilon *et al.* [2014] or Jin *et al.* [2015].

## 4. Seismicity

### 4.1. Methods and Data Analysis

Earthquakes are detected and located for the period March 2010 to January 2011 when both the land and marine seismometers were operating, applying the procedures of Li *et al.* [2013] summarized here. For the purposes of event detection the vertical component seismograms for land-based stations are band pass filtered at 2–8 Hz, from which short-term and long-term mean square amplitudes are calculated in windows 2 and 20 s long, respectively. Detections are declared when the short-term to long-term energy ratio exceeded 3.5, giving 266,782 detections. The OBSs are not used in this initial step owing to their significantly different noise characteristics. A grid of candidate locations is tested against the detections whenever at least

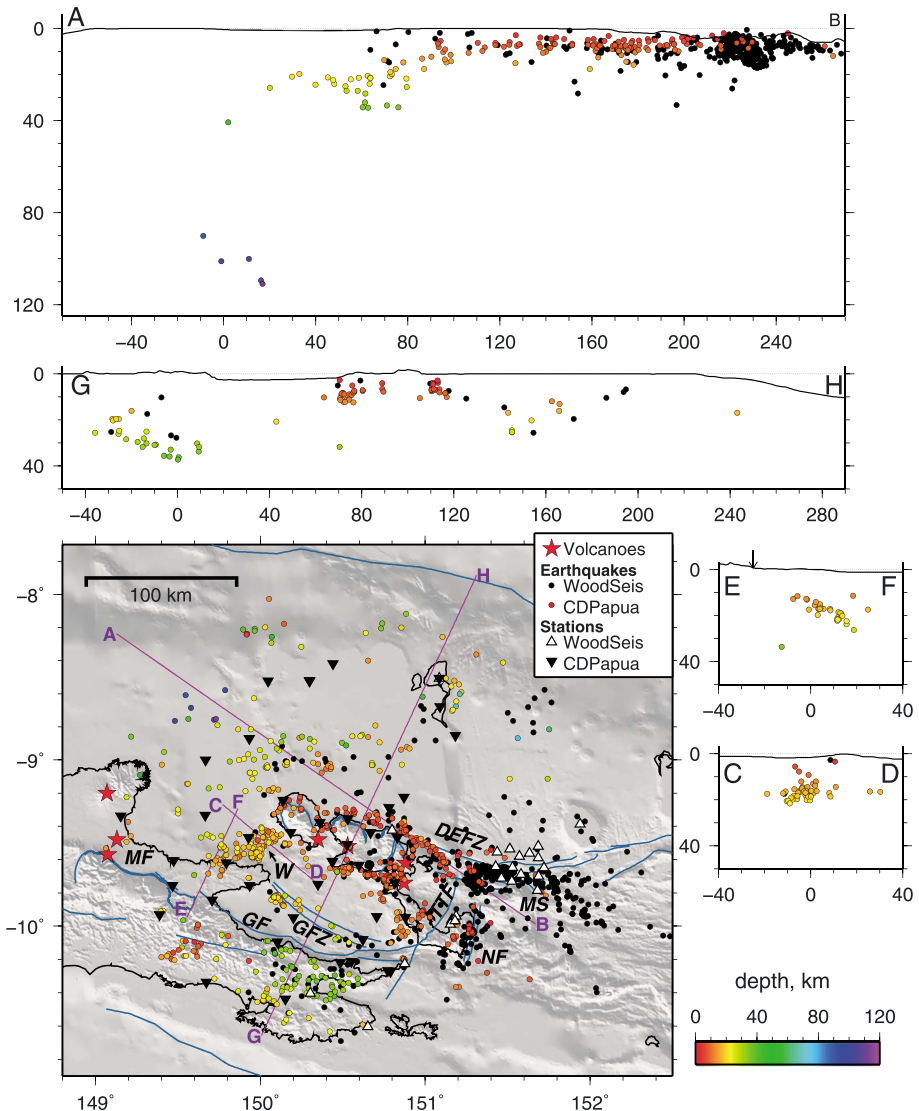


**Figure 2.** Microseismicity determined from regional arrays, from CDPAPUA (colored dots) and WOODSEIS (black dots). All relocations redetermined by HypoDD [Walshauer and Ellsworth, 2000] as described in text. For the CDPAPUA hypocenters, depths are color coded as per lower right scale bar. Abbreviations are MF: Mai'u Fault, W: Ward Hunt Strait Fault Zone, GF: Goodenough Bay Fault, GFZ: Goshen Fault Zone [Mutter et al., 1996], DEFZ: D'Entrecasteaux Island Fault Zone, TTF: Trobiand Transfer Fault [Little et al., 2011], NF: Normanby Fault [Little et al., 2007], and MS: Moresby Seamount. Cross sections are shown in other panels as labeled; topography exaggerated two times and dotted line shows sea level. Arrow on E-F indicates surface trace of Mai'u Fault. Earthquakes are projected  $\pm 10$  km from locations of cross sections shown on map, except for A-B where projection is  $\pm 25$  km.

five arrivals matched  $P$  or  $S$  predicted times within 5 s. Of these associations, 2952 potential events are located within  $2.5^\circ$  of the center of the array. These are manually repicked from the unfiltered data, adding OBS data and  $S$  wave picks from horizontal components and deleting nonearthquake signals. The final catalog of 795 earthquakes (7419  $P$  and 5735  $S$  picks) includes only hypocenters with horizontal and vertical formal errors for single-event locations less than 5 km and 7 km, respectively (Figure 2). These earthquakes are located in a one-dimensional velocity model determined from the WOODSEIS seismic array [Ferris et al., 2006, Table 1], merged with WOODSEIS arrival times, and jointly relocated in the same velocity model with the double-difference relative location scheme hypoDD [Walshauer and Ellsworth, 2000]. Clustering parameters in hypoDD were set to maximize connectivity between event pairs at tens of kilometers distance and minimize the number of events removed, given the widespread and diffuse nature of seismicity here, although some

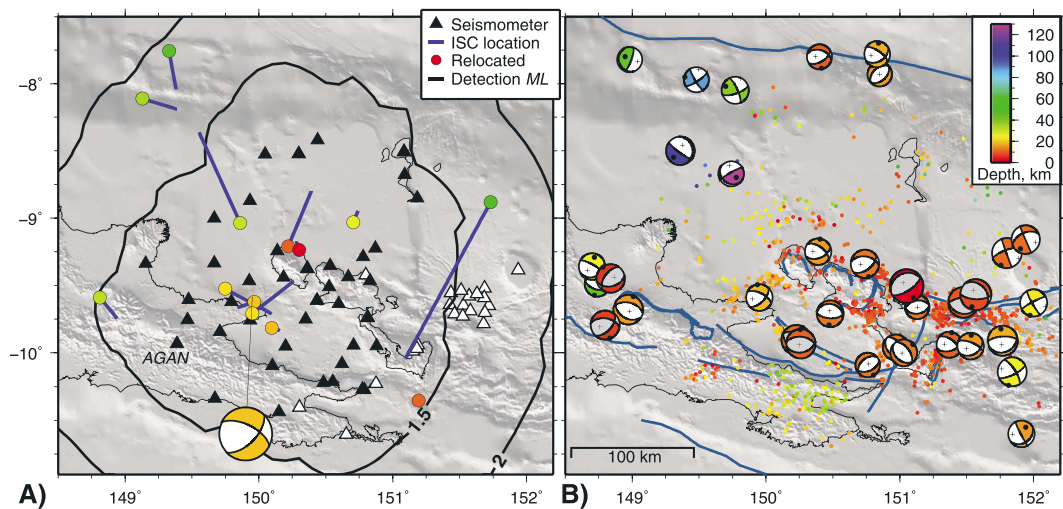


**Figure 3.** (a) Comparison of CDPAPUA to ISC catalog, 2010–2011. Circles show 14 earthquakes common to both catalogs at CDPAPUA epicenters, colored by relocated depth. Blue lines connect them to the corresponding ISC epicenter. Beach ball shows gCMT best double-couple solution for the one earthquake common to CDPAPUA and the gCMT catalog. Contours show detection limits for  $M_L = 1.5$  and 2.0. Triangles show stations, open for older WOODSEIS stations not used in detection analysis. (b) Relocated CDPAPUA seismicity and double-couple focal mechanisms from the gCMT catalog [Ekström et al., 2012] and, for older events, from body wave inversion [Abers et al., 1997]. The latter are indicated by gray dilatational quadrants. Compressional quadrants and epicenters are colored by depth; scale in inset.

isolated events past the edges of the array were discarded. Compared with single-event locations, the relative relocation slightly decreased the range of depths and decreased scatter in seismicity. Single-event locations for all locatable earthquakes are shown in the supporting information Figure S2a.

Fourteen of the earthquakes located here also appear in the International Seismological Centre (ISC) global catalog [International Seismological Centre, 2013]. The 14 ISC epicenters deviate from those here by 5 to 147 km with a median difference of 26 km but no statistically significant bias (Figure 3a). These shifts greatly exceed our formal errors but lie within reported uncertainties of ISC epicenters for these events, which range from 5 to 293 km. Errors of tens of kilometers are probably typical of global catalogs for poorly monitored regions of the globe. One earthquake recorded by CDPAPUA near Cape Vogel was large enough (ISC  $m_b = 5.4$ ; CDPAPUA  $M_L = 5.43$ ) to be analyzed by the Global Centroid Moment Tensor (gCMT) Project [Ekström et al., 2012].

In order to assess spatial variation in network detection,  $M_L$  magnitudes for all earthquakes are calculated from horizontal component signals, filtered to a Wood-Anderson instrument response, and measured using standard formulas and calibrations [Richter, 1935]. The resulting catalog has 317 earthquakes with  $M_L > 2.0$  and 10 earthquakes with  $M_L > 4.0$ ; 73% of the catalog has  $M_L > 1.5$ . This measurement is not calibrated to regional propagation conditions, but comparison with global catalog magnitudes for the 14 events did not reveal any obvious systematic bias greater than 0.2 magnitude units (Figure S2d). To estimate detection thresholds, we calculate a detection-limit curve of the form  $M_{\min}(R) = a + bR + c \log(R)$  such that 95% of all measured single-station  $M_L$  exceed  $M_{\min}$  at its corresponding source-receiver distance  $R$ , binned each 0.1 log units (Figure S2b). Linear regression is used to estimate coefficients  $a$ ,  $b$ , and  $c$ . At each latitude and longitude the completeness threshold  $M_C$  was set to  $M_{\min}(R)$  for the fourth closest station, since a minimum of four stations are needed to locate an earthquake. The analysis for CDPAPUA shows detection of  $M_L \geq 1.5$  extends throughout the region of MCCs from the south coast of the Papuan Peninsula to the Trobriand Trough (Figure 3a).

## 4.2. Results

### 4.2.1. Fault Zones Outlined by Seismicity

Hypocenters outline a belt of crustal deformation extending westward from the oceanic rift tip at 151.7°E (Figure 2). Most shallow earthquakes ring Goodenough and Fergusson Islands following inferred or mapped

faults bounding the metamorphic core complexes [e.g., Davies and Warren, 1988; Little et al., 2011]. The most active earthquake zone, termed here the D'Entrecasteaux Fault Zone, extends from the oceanic rift tip and north of the Moresby Seamount low-angle normal fault [Taylor and Huchon, 2002] to the north coast of Fergusson at 150.9°E and includes the largest ( $M > 6$ ) earthquakes in the region (Figure 3b).

Earthquakes also outline several previously reported fault systems, such as the Normanby Transfer Fault zone along the east coast of Normanby Island at 151.3°E [Little et al., 2007], which transfers some extension from the spreading tip to faults near the Papuan Peninsula, the Goshen Fault Zone in the central Goodenough Basin observed in seismic reflection data [Mutter et al., 1996; Fitz and Mann, 2013], and portions of the Trobriand Transfer Fault that crosses Normanby Island [Little et al., 2011] although that fault clearly does not offset the D'Entrecasteaux Fault System. Earthquakes also follow the south coast of Fergusson Island, suggesting that the mapped south dipping fault zone [Hill et al., 1992] is active. Some of that seismicity may be associated with volcanic centers, particularly in Dawson Strait between Fergusson and Normanby Islands. Block boundaries in GPS inversions generally follow the seismicity [Wallace et al., 2014].

Intense seismicity occurs between the southeast corner of Goodenough Island and the Cape Vogel Peninsula. Close inspection reveals that this seismicity is on at least two connected faults. West of 149.9°E earthquakes lie just north of the Cape Vogel coastline, beneath the southern Kiribisi Basin, along a surface that dips gently to the north at 30–40° (Figure 2, cross-section E-F). That seismicity projects southward to the surface at the Mai'iu fault (arrow on cross-section E-F) so is likely the downdip extension of that fault. Seismicity in this region east of 149.9°E forms a diffuse swath crossing Ward Hunt Strait between Cape Vogel and Goodenough Island (Figure 2, cross-section C-D) and is named here the Ward Hunt Strait Fault Zone ("W" in Figure 2). A bathymetric high in this strait shows evidence for faults that disrupt reflectors on multichannel seismic lines [Fang, 2000] and shows the surface expression of the fault zone. Most earthquakes in the eastern zone crossing Ward Hunt Strait are aftershocks of a  $M_w = 5.4$  earthquake that shows oblique transtensional slip in global catalogs (Figure 3a). Earthquakes align weakly with the northeast striking fault plane of this focal mechanism indicating right-lateral slip on a northeast striking transfer fault, although it is difficult to resolve the fault plane. This sense of slip is consistent with the Kiribisi Basin moving north-northeast relative to the Goodenough Basin and with normal faulting on the Mai'iu fault inferred west of 149.9°E.

#### 4.2.2. Depth Distribution of Seismicity

Along the axis of the D'Entrecasteaux Fault Zone most earthquakes are  $< 20$  km deep. Crustal seismicity lies beneath the Papuan Peninsula at middle to lower crustal depths of 20–40 km (Figure 2, cross-section G-H). Scattered seismicity is found at all crustal depths beneath the Trobriand Platform. Given the sparse station spacing at the edges of the array, it is not clear how robust is the apparent northward deepening of seismicity.

About 75 km northwest of Goodenough Island, near 8.7°S, 149.7°E, a handful of earthquakes lie at intermediate depths of 90–120 km. Earthquakes at similar depths were detected farther west outside of the network (Figure S2), but those earthquakes did not form links to others in the double-difference processing so were discarded. The earthquakes are well recorded by the OBSs above them, and all have at least one station within 40 km of the epicenter, leading to formal errors for single-event locations less than 1.5 km in depth and less than 3.0 km horizontally for earthquakes located by at least 10 phases. Thus, it is highly unlikely that these earthquakes are mislocated in depth more than a few kilometers and so constitute a distinct new seismic zone. The intermediate-depth earthquakes are the first well-located subcrustal earthquakes within the Woodlark-D'Entrecasteaux Rift region, possibly extending the zone of intermediate-depth earthquakes that occur 200 km farther west beneath the center of the Papuan Peninsula [e.g., Abers and Roecker, 1991; Pegler et al., 1995]. The gCMT catalog includes two earthquakes in this cluster (Figure 3b).

## 5. Imaging Crustal Structure

To complement the seismicity and deformation analysis, we analyze velocity structure to gain insight into crustal thickness, composition, and temperature. We jointly invert receiver functions and surface-wave dispersion curves for crustal shear wave velocity and interface depths.

### 5.1. Methods and Data Analysis

#### 5.1.1. Data Preparation

To generate receiver functions, we examine teleseismic  $P$  waves from earthquakes with magnitude above 5.5 at 30–90° epicentral distance and with clear  $P$  on the horizontal component seismograms (generally, signal-to-noise

ratios  $>5$ ). Data are detrended, rotated, and filtered (three-pole Butterworth at 0.01–0.5 Hz). Vertical component records are deconvolved from corresponding radial records by an iterative time domain scheme [Ligorria and Ammon, 1999]. The deconvolution smooths over a Gaussian pulse of width parameter 2.0, equivalent to a 0.45 Hz characteristic frequency. The resulting receiver functions are linearly stacked in two back azimuthal bins, after removing obviously unstable results. One bin spans 90–180° back azimuth (mostly 90–135°) from the Tonga-New Zealand region, resulting in 2–12 traces per station. The other bin spans 270–360° back azimuth (mostly 315–360°) from the northwest Pacific source region, with 3–39 traces per station. Each stacked receiver function is assigned the average ray parameter for that bin, to allow for spatial variation in signals. A total of 745 receiver functions are calculated, on average 11.0 per OBS station and 24.3 per land station. Receiver functions are successfully recovered for 6 OBS stations and 28 land stations.

Complementary surface-wave dispersion curves are described in a separate study [Jin *et al.*, 2015], summarized here. Fundamental mode Rayleigh wave phase velocities were measured from both ambient noise and earthquake signals at 10–60 s periods. At periods less than 20 s, a frequency domain method was used to derive phase velocities from ambient noise correlation [Menke and Jin, 2015]. Helmholtz tomography was used to derive phase velocity maps at longer periods, from earthquake signals [Jin and Gaherty, 2015]. Phase velocity maps for each period are interpolated to each station location and combined to provide a dispersion curve for the fundamental mode Rayleigh wave.

### 5.1.2. Joint Inversion

Receiver functions are jointly inverted with Rayleigh wave phase velocities using a transdimensional Bayesian scheme [Bodin *et al.*, 2012] as implemented by Obrebski *et al.* [2015] to estimate a single flat-lying structure beneath each station from the two receiver function stacks and single dispersion curve. The transdimensional Bayesian inversion simultaneously solves for thickness and shear velocity ( $V_S$ ) of flat layers through Monte Carlo simulation. The number of layers is treated as a free parameter along with noise levels, in a manner that tends to find solutions that minimize the number of layers needed to describe data [Malinverno, 2002]. The approach does not otherwise impose any smoothing, damping, or other regularization between layers. Attempts to solve for  $V_P/V_S$  led to considerable trade-offs between parameters and generally larger uncertainties, so instead, we fix  $V_P$  to  $V_S$  following an assumed relationship. Specifically, we set  $V_P = 1.80V_S$  for  $V_S > 2.125$  km/s and  $V_P = 1.16V_S + 1.36$  km/s for  $V_S < 2.125$  km/s, the latter being the “mudline” curve [Castagna *et al.*, 1985] appropriate for porous silicic sediments with low  $V_S$ . Tests of other scaling values at  $V_S > 2.125$  km/s do not significantly change the data misfit or first-order structure. They produce essentially identical  $V_S$  away from interfaces and a small trade-off between  $V_P/V_S$  and interface depth; an increase in  $V_P/V_S$  of 0.1 results in a 1.5 km decrease in Moho depth.

We adopt the convergence scheme, noise models, and weighting of Obrebski *et al.* [2015], although we experimented with alternative formulations for noisier OBS data. Randomly perturbed models are successively tested and compared with the previous best fit model and are accepted if they improve the fit or if randomly selected according to the convergence criteria. This process is repeated for 500,000 Monte Carlo simulations where the last 80% of the acceptable models contribute to the probability density function (pdf) of the inversion parameters; for efficiency only a randomly selected 1% of the accepted models are saved. The best estimate velocity at each depth is the maximum-likelihood  $V_S$  at the peak of the pdf. Figure 4 shows an example of the fitting and inversion results from station AGAN (location on Figure 3a); Figure S3 shows inversion results for all stations. The inversion produces a pdf for  $V_S$  as a function of depth, a pdf for interface depth, and a pdf for the number of layers (Figures 4c–4e). In this example the inversion favors four to six layers with a well-defined Moho and complex upper crustal structure.  $V_S$  estimates in the middle to lower crust are not unique since maxima exist at both 3.45 and 3.7 km/s, presumably trading off with near-surface velocities. The location of the Moho is well resolved to 3 km at 95% confidence ( $1\sigma$  uncertainty of 0.76 km), because surface-wave phase velocities place strong constraints on integrated crustal velocity. Like many sites, the upper 10 km shows a wide range in possible  $V_S$  that can match phase velocity constraints, all lower than 3.5 km/s. The model fits well the upgoing P-to-S ( $P_S$ ) arrival on the receiver functions (6 s lag time, Figure 4a), but the primary reverberations at 16–22 s lag are not consistently observed between the two back azimuths so cannot be fit. Such inconsistencies explain why inverting for  $V_P/V_S$  was not successful. The variation between back azimuth, also seen at an early conversion at 3 s lag, indicates that these are not robust features of one-dimensional structure but are complicated by crustal heterogeneity.

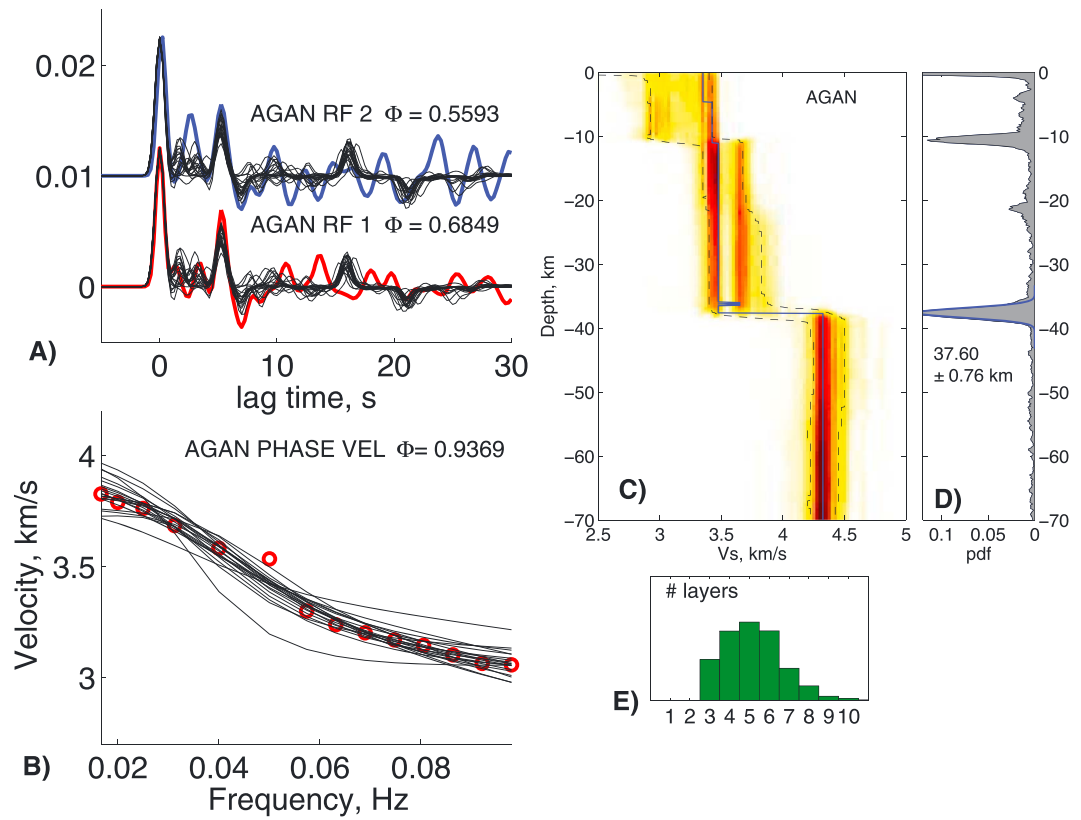


**Figure 4.** Example of velocity inversion for station AGAN (see Figure 3a). (a) Receiver functions for two back azimuths, 90–135° (bottom) and 315–360° (top); colored lines show stacked data, and thin black lines show best fit model predictions. (b) Phase velocities for fundamental mode Rayleigh waves.  $\Phi$  denotes misfit measure. Red circles are observed data, and black lines show best fit predictions. Figures 4a and 4b show a randomly selected 20 of the 2000 best fitting models. (c) Pdf for  $V_S$  with depth; darker colors indicate higher probability. Dashed lines bound the central 80% of acceptable models. (d) Probability density function (pdf) for interface depth; peaks show most likely depths for interfaces. The Moho is picked from the peak as described in the text, here assigned a depth of  $37.60 \pm 0.76$  km ( $1\sigma$  uncertainty in local maximum probability). (e) Pdf for number of layers in the best fitting model.

### 5.1.3. Moho Depth

The base of crust (Moho) is equated with the discontinuity below which nominal mantle velocities were reached ( $V_S > 4.0$  km/s generally) and set to the local peak in the marginal pdf for interface depth (e.g., 37.6 km in Figure 4d). In cases where multiple discontinuities or a gradational velocity increase was present, the Moho is assigned to the deepest interface above which velocities with  $V_S < 4.0$  km/s occurred. For OBS data in the Kiribisi Basin this assignment is particularly difficult because formal velocity uncertainties were large; the 80% confidence range was  $>0.4$  km/s wide. Formal errors are derived from the half width of a Gaussian function fit to the pdf peak, which seem adequate in cases where the peak is strong but seem to give low uncertainties otherwise.

As an alternative assessment of the Moho depth accuracy, we numerically calculate the pdf for  $dV_M$ , the  $V_S$  step across the Moho (measured between 5 km below and 5 km above the Moho). The pdf for  $dV_M$  is integrated over all positive values to estimate the probability that the velocity step is positive, i.e., that  $P(dV_M > 0)$ . This probability measures the significance and reliability of the Moho peak and is used to scale Moho depth symbols (Figure 5).

### 5.2. Results

The  $V_S$  estimates are shown at three depths and one crustal average from the individual station pdfs and averaged over groups of nearby stations (Figure 6). Stations on the Trobriand Platform show  $V_S$  of 1–3 km/s in the uppermost 2–3 km (Figure 6e), consistent with sediment thicknesses drilled there [Taylor and Huchon, 2002].

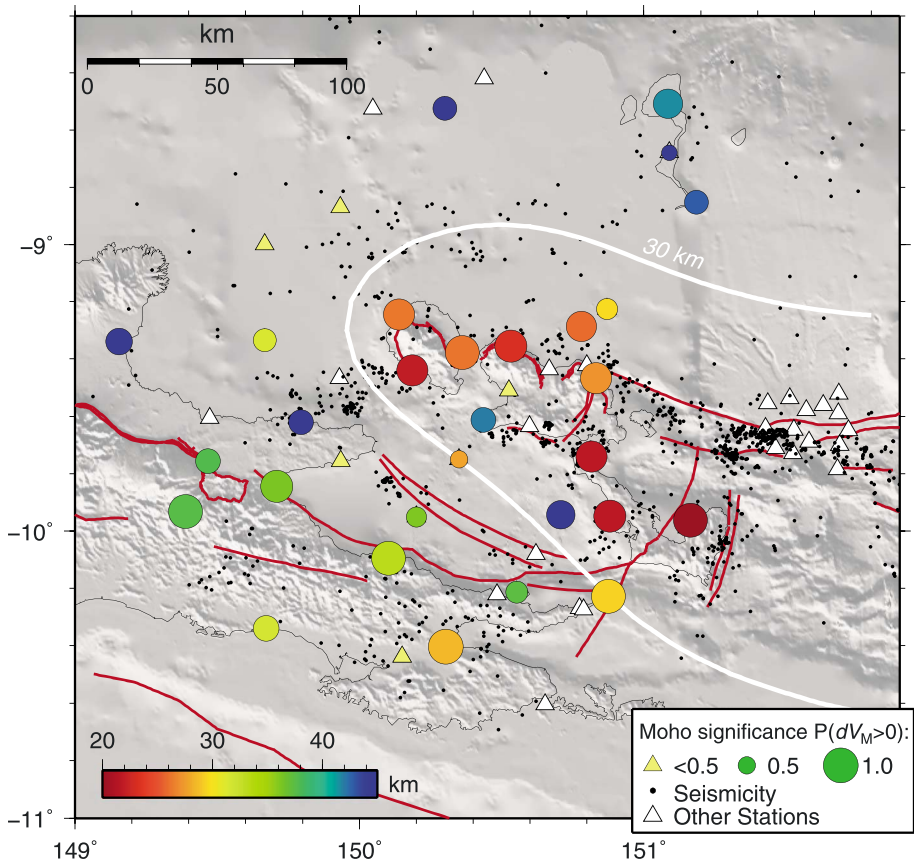


**Figure 5.** Crustal thickness below each station determined from joint inversions. Circles, colored by best fitting Moho depth, are scaled to  $P(dV_M > 0)$  the fraction of successful models for which the Moho velocity step  $dV_M$  is positive. Triangles show stations for which  $P(dV_M > 0)$  is less than 0.5 (yellow), or no receiver functions could be determined (open). Black dots show relocated seismicity. White line shows approximate 30 km depth contour from fitting third-order polynomial surface to these data.

The upper crust at 8 km depth has 90% of the  $V_S$  between 3.0 and 3.6 km/s averaging 3.34 km/s, with outliers corresponding to noisy stations with uncertainties  $\geq 0.3$  km/s (Figure 6a). Velocities are generally slowest beneath the Papuan Peninsula and the northern D'Entrecasteaux Islands. For  $V_P/V_S = 1.75\text{--}1.80$  the  $V_S$  range corresponds to  $V_P = 5.3\text{--}6.5$  km/s. Globally,  $V_P$  in rifts average 5.6 and 6.1 km/s at 5 and 10 km depths, respectively [Christensen and Mooney, 1995], similar to the observations here.

Lower crustal shear velocities at 20 km depth average 3.67 km/s with two population peaks near 3.5 and 3.9 km/s (Figure 6b). The low- $V_S$  lower crust is concentrated along the D'Entrecasteaux Islands and a few sites on the Papuan Peninsula, while the highest  $V_S$  lies beneath the Goodenough Basin and Trobriand Platform (the easternmost D'Entrecasteaux Island site on Normanby shows fast velocities at 20 km depth, but the crust there is only 17.3 km thick). Mean crustal velocities, calculated to exclude low-velocity sediment ( $V_S < 2.5$  km/s; Figure 6c), show a clearer pattern of low  $V_S$  ( $\leq 3.5$  km/s) along the D'Entrecasteaux Islands and the northern Papuan Peninsula and higher  $V_S$  ( $> 3.65$  km/s) elsewhere. At 10–25 km depth the D'Entrecasteaux Islands sites are 0.1 km/s slower than those on the Papuan Peninsula, with considerable overlap, while the Trobriand Platform is 0.2–0.3 km/s faster (Figure 6e). The mean crustal  $V_S$  averages 3.5 km/s with modal peaks at 3.45 and 3.7 km/s. Average  $V_P$  for rifts and extended crust globally are 6.5 km/s at 20 km depth [Christensen and Mooney, 1995] consistent with  $V_S$  of 3.6–3.7 km/s for  $V_P/V_S = 1.75\text{--}1.80$ , in excellent agreement with the higher peak in Figures 6b and 6c.

The uppermost mantle ( $V_S$  taken 5 km below Moho) shows similar patterns as the lower crust, with low velocities along the rift axis (3.9–4.2 km/s) and high  $V_S$  on either side (4.3–4.5 km/s) and a median  $V_S$  of 4.3 km/s.

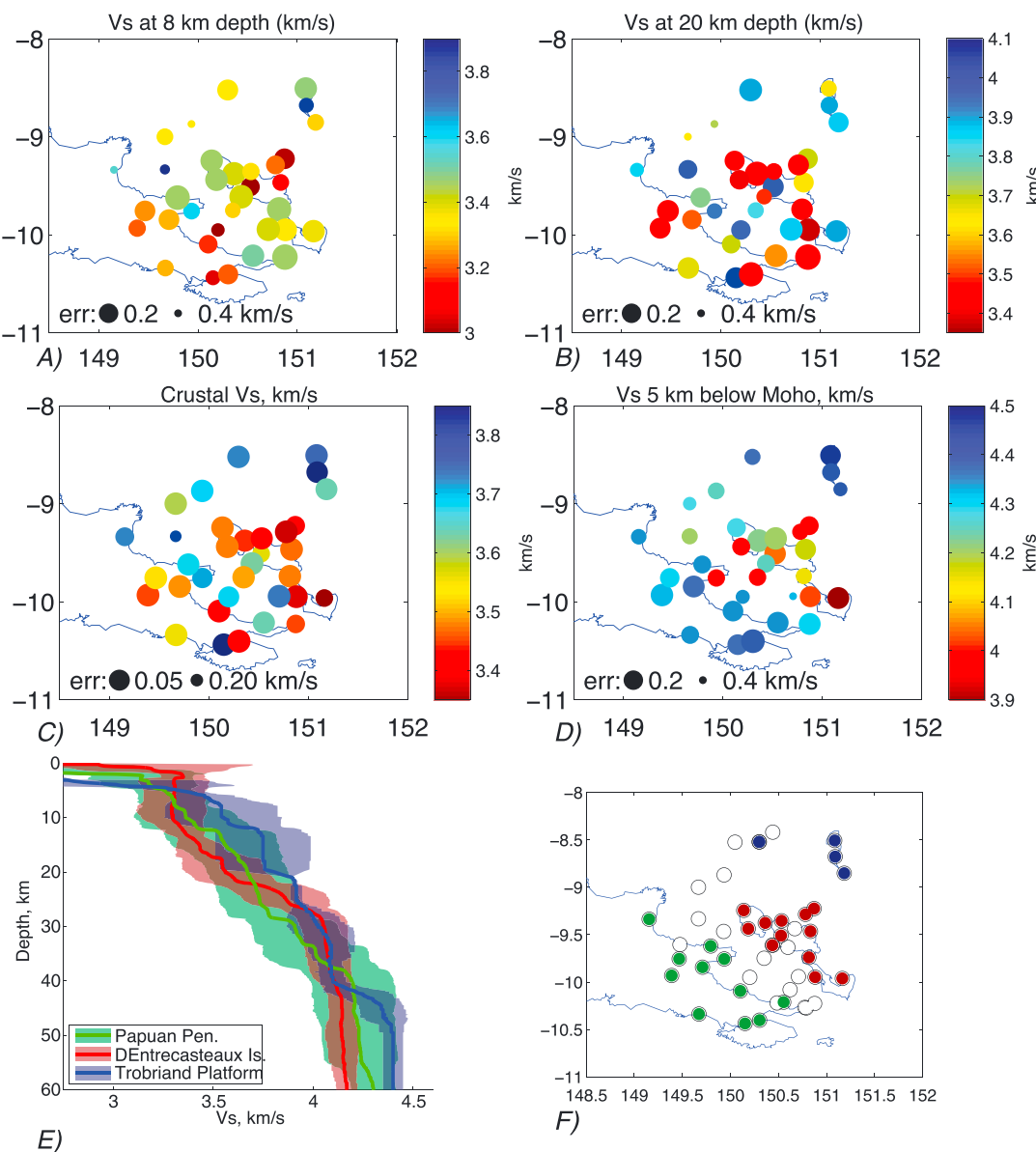


**Figure 6.**  $V_s$  at different depths. (a) Upper crust at 8 km depth. (b) Lower crust at 20 km depth. (c) Mean crustal  $V_s$  above Moho, averaged as  $1/V_s$  to preserve travel times. Only depths where  $V_s > 2.5$  km/s are included in averages to remove effects of near-surface sediment. (d)  $V_s$  5 km below Moho. For Figures 6a–6d, symbol size scales inversely to formal error as shown; error represents 80% probability range. (e)  $V_s$  versus depth averaged over groups of stations, as indicated by key. Solid shading indicates  $1\sigma$  variation in  $V_s$  between stations in the same group. (f) Stations used in groupings for Figure 6e as indicated by color; open circles indicate stations not used.

This pattern is largely driven by surface-wave dispersion at periods of 20 s and longer and is discussed by Jin *et al.* [2015].

The Moho varies considerably in depth and strength (Figure 5). Crustal thickness beneath the D'Entrecasteaux Islands is 25–30 km for most sites decreasing to 17 km at easternmost parts of Normanby (Figures 7a and 7b), consistent with limited previous data [Abers *et al.*, 2002]. In most cases these stations exhibit a sharp Moho with a velocity discontinuity of 0.5–0.9 km/s. Crustal thicknesses in the Amphlett Islands (Pliocene volcanic centers just northeast of Fergusson) are similar. The Papuan Peninsula has generally thicker crust of 35–40 km, with sites farthest west exhibiting complex structure and reaching 45–55 km thickness. The four stations on the northern Trobriand Platform show similar receiver functions as each other, featuring crustal thickness of 42–49 km and gradational lower crustal  $V_s$ . Overall, the crust is 20 km thinner beneath the D'Entrecasteaux Islands than to the north and 10–15 km thinner than the Papuan Peninsula.

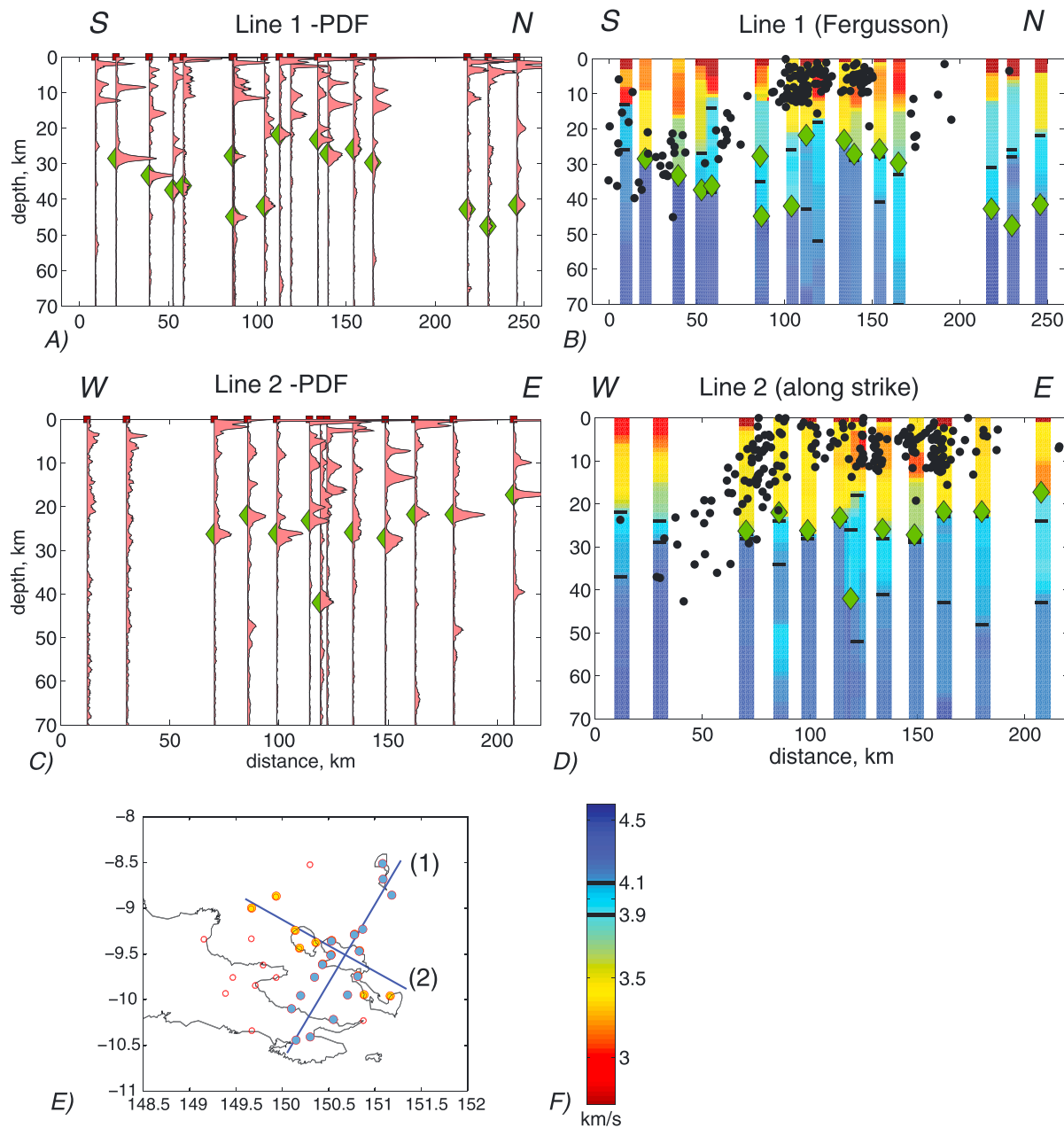


**Figure 7.** Cross sections of joint inversion results. (a and b) Cross section (1) through Fergusson Island. (c and d) Cross section (2) through Dayman Dome and Kiribati Basin. (e) Locations of cross sections, stations colored if used in cross sections (1). (f) Color scale for velocities shown in Figures 7b and 7d. Figures 7a and 7c are pdfs for interface depth beneath each station. Figures 7b and 7d show V<sub>S</sub> columns beneath each station, with horizontal bars corresponding to V<sub>S</sub> = 3.9 and 4.1 km/s and seismicity within 35 km of the section as black dots. Green diamonds on Figures 7a–7d indicate maximum-likelihood interface depth identified as Moho, in cases where dV<sub>M</sub> > 0.25 km/s (velocity contrast  $\pm 5$  km from interface).

In some cases Moho is difficult to discern, as evident as a small  $dV_M \leq 0.5$ . Generally, these stations exhibit complex signals such as caused by basin reverberations, common in the OBS data.

## 6. Discussion

### 6.1. Fault Zone Geometries, Transfer Structures, and Locus of Extension

Most microearthquakes (Figure 2) and large earthquakes (Figure 3b) lie along and around the D'Entrecasteaux Islands or in seismicity zones extending east and west from them. East of 151.7°E deformation is highly localized

at the oceanic rift axis; the seismicity between the rift tip and about 150.6°E (120 km west) is largely concentrated along fault systems collinear with the rift. The D'Entrecasteaux Fault Zone seismicity begins at the oceanic rift tip (9.7°S, 151.7°E) and continues west-northwest without offset or break around the north coast of Fergusson Island, although the trend deflects around the main MCC domes, and extends to northern Goodenough Island (Figure 2). All focal mechanisms in this zone show normal faulting with roughly north-south  $T$  axes (Figure 3b). The simplest interpretation is that deformation is continuous along an interconnected set of currently active normal faults and transfer structures making up the D'Entrecasteaux Fault Zone. Seismicity also reveals fault zones crossing Normanby Island and beneath the eastern Papuan Peninsula, consistent with some fraction of plate motion occurring south of the MCCs as indicated by GPS data [Wallace *et al.*, 2014]. Seismicity on the south side of Fergusson lies along a coastline that shows geomorphic evidence for the present activity [Miller *et al.*, 2012].

While most seismicity corresponds to previously identified fault zones [e.g., Little *et al.*, 2007, 2011], abundant seismicity lies just north of Cape Vogel. The western part of this seismicity, west of 149.9°E, forms a planar surface dipping north at 30–40° that is the downdip extension of the Mai'i'u Fault at the foot of Dayman Dome (Figure 2, cross-section E-F). Earthquakes extend to a maximum of 20–25 km depth, similar to many continental rifts worldwide [Ruppel, 1995; Abers, 2001] although deeper than earthquakes flanking the D'Entrecasteaux MCCs, presumably reflecting lower midcrustal temperatures along the Mai'i'u fault. Seismicity east of 149.9°E forms the Ward Hunt Strait Fault Zone and shows unclear internal structure (Figure 2, cross-section C-D), but the overall geometry strongly resembles a northeast-southwest trending transform fault offsetting two normal fault systems. Similar oblique transfer fault systems exist in many rifts [Gawthorpe and Hurst, 1993], for example, in East Africa [Ebinger, 1989] and western North America [Burchfiel *et al.*, 1987]. We interpret the Ward Hunt Strait Fault Zone as a similar transfer zone linking extension between the Mai'i'u Fault and the D'Entrecasteaux Fault Zone. Documentation of this transfer zone resolves a paradox in regional kinematics: although the D'Entrecasteaux Fault Zone shows much evidence for rapid modern motion [Abers, 1991; Baldwin *et al.*, 2004; Miller *et al.*, 2012; Wallace *et al.*, 2014], the Kiribisi Basin immediately to the west is virtually undeformed and shows only a couple kilometers of extension [Fitz and Mann, 2013]. The existence of a transfer structure allows large extension across Goodenough Island without disrupting adjacent basin strata.

The Mai'i'u Fault bounding the Dayman Dome probably accommodates most of the extension west of 150°E, but eastward the locus of the greatest extension migrates north to the D'Entrecasteaux Islands at Ward Hunt Strait rather than continuing along the north Papua coast. Roughly 5–8 mm/yr geodetic extension has been modeled along the Papuan Coast at the Goodenough Bay Fault near 150°E [Wallace *et al.*, 2014]. However, the geodetic estimate assumes that Cape Vogel lies on the same block as the Goodenough Basin and does not account for motion on the Ward Hunt Strait Fault Zone. Owing to deformation transferred by this structure, it seems likely that motion on the Mai'i'u Fault at the Dayman Dome could be significantly larger west of 149.8°E than motion on the Goodenough Bay Fault farther east. Supporting such a gradient in displacement, stream incision rates appear much lower on the footwall east of Cape Vogel than along the Dayman Dome [Miller *et al.*, 2012], following seismicity rates. This deformation geometry might be a relatively recent phenomenon; regionally consistent knickpoints in stream profiles indicate the onset of an incision event in the Pleistocene [Miller *et al.*, 2012], and seafloor fabric within the oceanic Woodlark basin indicates a reorientation of plate motion at  $\leq 0.52$  Ma [Goodliffe *et al.*, 1997].

Little crustal seismicity is observed that could be associated with proposed south dipping subduction at the Trobriand Trough [e.g., Taylor and Huchon, 2002], even though detection should be complete for  $M_L \geq 2.0$  at the trough and  $M_L \geq 1.5$  beneath the northern part of the array where a likely megathrust should lie. Sparse subcrustal seismicity is observed northwest of Goodenough Island reaching 120 km depth, but none of the published focal mechanisms show thrust faulting (Figure 3), and the scattered hypocenters on the Trobriand Platform do not lie consistently at plate interface depths. Geodetic data also suggest that the Trobriand Trough is currently inactive or extensional [Wallace *et al.*, 2004, 2014], so we infer that any convergence here happened before 0.52 Ma or earlier.

Microseismicity beneath the Papuan Peninsula defines a surface dipping to the north-northeast at 20° at 20–35 km depth (Figure 2, cross-section G-H). Unfortunately, no focal mechanisms could be determined for these earthquakes. While it is possible that this is a north dipping fault surface reaching the surface near the Pocklington Trough, the GPS sites on the Papuan Peninsula show virtually no motion with respect to

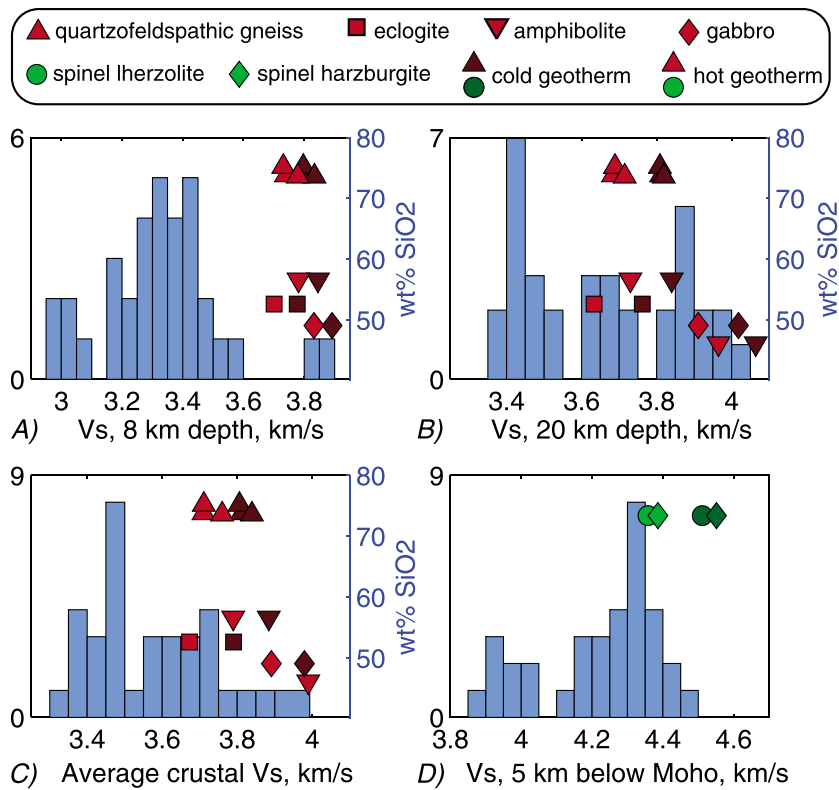


**Figure 8.** Histograms of  $V_s$  for all depth ranges and stations shown in Figure 6. Symbols show  $V_s$  predictions from different lithologies, plotted against wt % SiO<sub>2</sub>. (a–c) Histograms of  $V_s$  at crustal depths (left axis) compared with predictions for crustal lithologies (symbols; right axis) from Brownlee et al. [2011] or Brooks and Tegner [2001] as described in text. (d) Uppermost mantle  $V_s$  and predictions for ultramafic rocks (symbols); compositions from Hacker et al. [2003]. Compositions are described in legend (top). Velocities are calculated [Hacker and Abers, 2004; Abers and Hacker, 2016] at the depths of 8 km in Figure 8a, 20 km in Figure 8b, average between Moho and base of layers with  $V_s < 2.5$  km/s in Figure 8c, and 40 km in Figure 8d. Two geotherms are assumed, a cold one with surface flux of 50 mW/m<sup>2</sup> (dark symbols) and a hot one with 150 mW/m<sup>2</sup> (bright symbols); see Figure 9. Calculations are for solid parts of rock only; small melt fractions could lower  $V_s$  substantially, depending on melt topology.

Australia [Wallace et al., 2014]. Rather, we suspect that this sharp truncation in seismicity marks a rheological boundary as a brittle-ductile transition, similar to that seen beneath the Gulf of Corinth [Hatzfeld et al., 2000]. The southeast Papuan Peninsula also experienced pre-late Miocene counterclockwise rotation of 12–28° [Cairns et al., 2015], so some inactive deformational structures should be present.

## 6.2. Composition of the Crust and Absence of PUB

To assess crustal composition, we predict  $V_s$  for well-documented lithologies in the region and compare them to observations (Figure 8). Brownlee et al. [2011] estimated modal mineralogy and elastic properties for a suite of rocks from the D'Entrecasteaux MCCs with SiO<sub>2</sub> contents varying from 46 to 75 wt % including quartzofeldspathic gneisses, amphibolites, and mafic eclogites. Gabbros drilled north of the Moresby Seamount and on the eastern Papuan Peninsula also are well described in terms of major element chemistry and are also included [Brooks and Tegner, 2001]. For each of these bulk compositions we calculate equilibrium phase assemblages from free-energy minimization via Perple\_X [Connolly, 2005] using the solution models and low-temperature disequilibrium assumptions of Brownlee et al. [2011]. Velocities are then calculated at elevated pressure and temperature [Hacker and Abers, 2004; Abers and Hacker, 2016]. At conditions that match Brownlee et al. [2011] we reproduce their results, but we explore additional geotherms. We also include two ultramafic lithologies, a spinel Iherzolite and a depleted spinel harzburgite [Hacker et al., 2003]. The peridotite  $V_s$  are corrected for anelasticity by scaling to the ratio of relaxed to unrelaxed  $V_s$  from Jackson and Faul [2010], assuming a 1 cm grain size and a period depth scaling appropriate for fundamental mode Rayleigh waves [e.g., Abers et al., 2014]; anelasticity corrections are <1% at <1000°C.

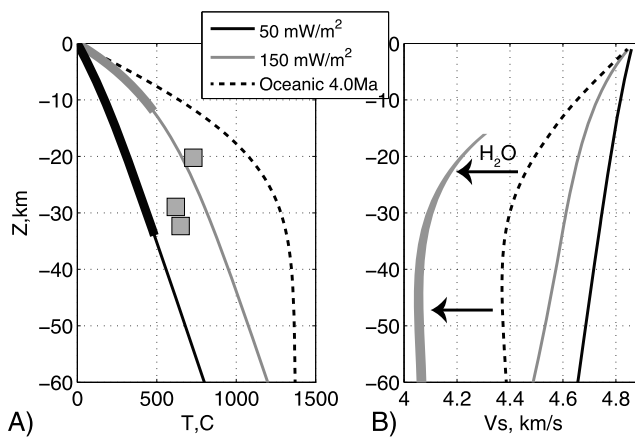


**Figure 9.** Geotherms and predicted mantle  $V_S$ . (a) Temperatures along a hot (gray) and cool (black) continental geotherm as described in text and a young oceanic geotherm (dashed) calculated for typical half-space cooling parameters, a 1350°C potential temperature, a plate age of 4 Ma, and 0.35 K/km adiabat [Turcotte and Schubert, 2002]. Gray squares show conditions estimated for 2–4 Ma metamorphic rocks in the D'Entrecasteaux MCCs [Hill and Baldwin, 1993]. Thick lines indicate depth range of seismogenic crust beneath the MCCs (gray) and Papuan Peninsula (black). (b) Corresponding anelastic  $V_S$  calculated along the three geotherms for dry olivine [Jackson and Faul, 2010], for typical mantle grain size of 1 cm, and at Rayleigh wave dominant periods of  $(3Z)/(4.2 \text{ km/s})$  where  $Z$  is depth [Forsyth, 1992]. Slower gray field shows mantle  $V_S$  estimate for the 4 Ma plate geotherm including effect of typical concentrations of  $\text{H}_2\text{O}$  in olivine (50 wt ppm) and equilibrium grain sizes appropriate for strain rates of  $10^{-14}$  to  $10^{-13} \text{ s}^{-1}$ , at temperatures  $> 900^\circ\text{C}$  where anelastic effects are calibrated and grain size equilibrium can be assumed (calculations described in Abers et al. [2014]).

predictions are 3.7–3.8 km/s, so none of these models match predictions. Such an underestimate commonly occurs in shallow rocks and probably reflects the influence of water-filled cracks and pores [Christensen, 1996; Brocher, 2005]. Seismicity at  $\leq 8$  km depth throughout the region suggests that temperatures are not sufficient to produce melt at this depth. Many of the lowest  $V_S$  values are on the Papuan Peninsula or in the Amphlett Islands (Figure 6). It is not clear why this would be the case, but most of those sites are characterized by a layered rather than the homogeneous crust below the D'Entrecasteaux Islands (Figure S3), so velocities are more gradational.

Observed  $V_S$  in the lower crust (Figure 8b) and crustal averages (Figure 8c) show greater overlap with calculated  $V_S$ . Predicted  $V_S$  of 3.6 to 4.1 km/s weakly anticorrelates with silica content, consistent with mafic to intermediate compositions in the lower crust. Observed velocities are matched for the Trobriand Platform, which shows uniformly high velocities, and perhaps Goodenough Bay. Measurements with  $V_S = 3.4$ –3.5 km/s at depths greater than 15 km are difficult to explain and conceivably require melt as water-filled pores should be closed at these depths; most of these measurements come from sites near Quaternary volcanic centers or young plutons in the D'Entrecasteaux Islands [Smith and Milsom, 1984]. Melt can have a strong effect on shear modulus and hence  $V_S$  [e.g., Hammond and Humphreys, 2000; McCarthy and Takei, 2011]. It is difficult to quantify the amount of melt needed to produce the observed maximum 5–15% reduction in  $V_S$  (Figure 8c), since  $V_S$ -melt relations vary by a factor of several depending upon how melt is distributed and interconnected [Schmelting, 1985]. At mantle conditions a 2–10% reduction in  $V_S$  occurs for each 1% increase in melt porosity (see discussion in Jin et al. [2015]), indicating 0.5–8% melt beneath the D'Entrecasteaux Island sites. Thus, a small amount of melt could produce sufficient velocity reductions. Volcanic systems may foster other phenomena that reduce velocities without melt, such as pervasive alteration and deep hydrothermal circulation.

Elsewhere, the crustal velocities appear to be typical of continents [e.g., Hacker et al., 2015]. Notably, the  $V_S$  observations preclude a significant volume of ultramafic rocks in the upper 20 km (4.5–4.8 km/s; Figures 7

Velocities are calculated along two geotherms designed to bound plausible temperatures (Figure 9), parameterized by a fixed surface heat flux  $q_0$  exponentially decaying rates of crustal heat production with e-folding depths of 10 km, and mantle heat flux of 30 mW/m<sup>2</sup> [Turcotte and Schubert, 2002, equation (4.31)]. The model is somewhat ad hoc but approximates typical continental geotherms over a range of conditions. A cold geotherm is calculated with  $q_0 = 50 \text{ mW/m}^2$  as observed in the Goodenough Basin, while a hot geotherm has  $q_0 = 150 \text{ mW/m}^2$  as observed near the D'Entrecasteaux Islands [Martinez et al., 2001]. The hot geotherm or one slightly colder also produces temperatures at 20–30 km depth similar to those estimated for <4 Ma high-grade metamorphic rocks nearby [Hill and Baldwin, 1993].

At a depth of 8 km the calculated  $V_S$  show little systematic variation over the full range of wt % SiO<sub>2</sub> (Figure 8). Most observed  $V_S$  are 3.2–3.5 km/s at this depth, while predic-

and 9b). The thick sections of the Papuan Ultramafic Belt and high crustal velocities found west of 148°W [Finlayson *et al.*, 1977] are absent here. Small outcrops of serpentinite and gabbros on the coastlines surround the core complexes [e.g., Davies and Warren, 1988; Little *et al.*, 2011], but it seems unlikely that these rocks represent a significant crustal fraction. Probably, the outcrops represent small slivers of related material caught in large displacement faults of the D'Entrecasteaux Fault Zone. The upper plate may resemble a melange with embedded fragments of serpentinite, similar in seismic properties to the Franciscan formation of California, which likewise shows slow shear wave speeds ( $V_S < 3.5$  km/s) in the upper 8 km [Lin *et al.*, 2010].

### 6.3. Inferred Buoyancy and Diapirism

Several observations here are at odds with diapiric ascent models for MCC formation. The conclusion that thick sections of PUB do not extend east of 149°E longitude conflicts with the suggestion that thick ultramafic sections in the upper crust generate a density inversion that drives diapiric ascent of crustal material to form MCCs [Martinez *et al.*, 2001; Fitz and Mann, 2013]. Density correlates with  $V_S$ , so the lack of velocity inversion can be taken as evidence for absence of density inversions within the crust. Since velocity inversions are also absent in the lower crust, it seems unlikely that felsic diapirs are underplating a more mafic crust.

The numerical models of Ellis *et al.* [2011] couple extension to diapirism without appealing to crustal density inversions. At least two effects probably produce buoyancy in these models. First, even after ascent the base of felsic diapirs lies deeper than the surrounding crust and produces positive buoyancy from what is effectively a crustal root beneath the MCCs; the diapirs extend deeper than the crust into which they intrude. This modeled feature is the opposite of what we observe: the crust is thinnest not thickest beneath the MCCs (Figures 5 and 7). Second, melt at shallow depths reduces density of the modeled felsic diapirs relative to surrounding felsic rock, and in the midcrust the modeled diapirs have up to 6% density decreases caused by very large (>40%) in situ melt fractions. Such large melt fractions are difficult to reconcile with seismic observations since they are probably too high to allow the passage of S waves [e.g., Schmeling, 1985; Mueller and Massonne, 2001], yet the MCC sites show uniformly large S waves in P-S conversions, so melt fraction is probably much less (see above). At 10–25 km depth the D'Entrecasteaux Islands are on average 2–4% slower in  $V_S$  than the Papuan Peninsula and 5–9% slower than the Trobriand Platform (Figure 6e), consistent with respective density differences of 1–2% or 2–4% given typical velocity-density relationships [Brocher, 2005]. Melt has a much larger effect on  $V_S$  than density so it is likely overestimates. Thus, the buoyancy of diapirs is probably small once it reaches crustal depths.

In the mantle, diapirs or coherent felsic blocks could occur as UHP rocks are exhumed [Ellis *et al.*, 2011; Little *et al.*, 2011; Petersen and Buck, 2015]. Small deep buoyant bodies may be invisible to seismic rays given the 25 km station spacing and 20–30 km Fresnel zone widths for 0.5 Hz S waves at 50–100 km depth, so that it is possible that mantle diapirs may exist at a scale smaller than the typical D'Entrecasteaux dome width. Alternatively, the absence of such bodies in seismic images may indicate that any diapirs beneath the array have already completed their journey and now lie within the lower crust. The flux rate from this process would have to be less than the extension in order to produce thin crust along the MCC axis.

The pattern of seismicity indicates a simple east-west striking system of normal faults connected by transfer faults, without any clear evidence for radial faulting. Some radial deformation late in the crustal metamorphic history of the MCCs seems necessary to explain radial patterns of lineation on the MCC surfaces [Little *et al.*, 2011]. However, such a deformation pattern is not evident in seismicity or focal mechanisms. Overall, the seismic observations do not obviously require diapiric ascent to control the dynamics of MCC formation, although they allow it as a secondary process.

### 6.4. Thermal Structure and Lithosphere Thinning

Low  $V_S$  in the crust of the D'Entrecasteaux Islands indicates high temperatures and cannot be explained by composition alone (Figures 6–8). Abundant volcanism [Smith and Milsom, 1984], high-measured heat flow [Martinez *et al.*, 2001], paleotemperatures of young exhumed rocks in MCCs [Baldwin *et al.*, 1993], and low upper mantle velocities [Abers *et al.*, 2002; Eilon *et al.*, 2015; Jin *et al.*, 2015] all support high temperatures beneath the D'Entrecasteaux Islands and potentially require complete removal of mantle lithosphere. Upper mantle  $V_S$  beneath the Papuan Peninsula and Trobriand Platform are in the range 4.4–4.5 km/s, consistent with temperatures at or exceeding 1000°C but not necessarily reaching typical asthenospheric temperatures (Figure 9) and not necessarily requiring the presence of melt or fluids. In general, mantle velocities less than 4.2–

4.3 km/s cannot be achieved in dry peridotites at normal mantle conditions even when anelasticity is taken into account for expected grain size of  $\geq 1$  cm [Abers *et al.*, 2014]. H<sub>2</sub>O in nominally anhydrous mantle minerals will lower velocities [Karato and Jung, 1998], and several wt % H<sub>2</sub>O have been observed in young basalts in the D'Entrecasteaux-Dayman region, indicating a damp upper mantle similar to beneath many arcs [Ruprecht *et al.*, 2013]. We estimate the effect of water by assuming the typical subarc mantle water and grain-sized conditions of Abers *et al.* [2014], and predict  $V_S$  of 4.0–4.1 km/s at asthenospheric temperatures (Figure 9b, gray field). The lower observed mantle  $V_S$  of 3.8–4.0 km/s observed beneath some D'Entrecasteaux Islands sites probably require the presence of melt, perhaps less than 1% [Jin *et al.*, 2015].

Earthquake depths provide an additional proxy for temperature. Earthquakes occur at depths less than 15–20 km along the rift axis (Figure 2), and waveform inversions indicate depths for large earthquakes <10–15 km (Figure 3b). By contrast, seismicity beneath the Papuan Peninsula extends throughout the crust to a depth of 35 km. The maximum depth of seismicity in quartz-dominated rocks should be limited by temperatures of approximately 350–450°C [Scholz, 1998], reached at depths of 25–32 km on the notional cold geotherm or 8–12 km on the hot geotherm. The maximum depth of seismicity lies close to 500°C along these geotherms, perhaps indicating a more mafic lithology (Figure 9a, thick lines) consistent with a more mafic basement to the Papuan Peninsula [Pigram and Davies, 1987]. Except as noted below, all of these earthquakes lie above the Moho as observed in other global compilations [Maggi *et al.*, 2000].

This relationship together with the observed Moho geometry indicates that the intense seismicity following the MCCs is likely to reflect a long-lived pattern of deformation. Both the differences in thermal gradient and the amount of crustal thinning require substantial crustal extension at the same place as modern seismicity. If the thickest crust of 45–50 km is taken as the prerifting crustal thickness, then restoring the Moho geometry of Figure 7a requires 34–53 km of extension, most of it beneath or close to the D'Entrecasteaux MCCs. The restoration explains only 1/3–1/2 of the extension at the longitude of Fergusson in the last 3.6 Ma expected from magnetic anomalies, perhaps indicating that simple models of crustal stretching cannot be applied here. The difference may, in part, reflect the addition of UHP material from mantle depth [Ellis *et al.*, 2011; Petersen and Buck, 2015].

It is not clear how to reconcile moderate crustal thinning with near-total removal of mantle lithosphere beneath the core complexes inferred from asthenospheric subcrustal  $V_S$ . This observation disagrees with simple pure shear-rifting models in which the Moho acts as a passive strain marker as the mantle lithosphere and crust thin in concert [McKenzie, 1978]. Models of depth-dependent extension suggested for this region [Kingdon and Goodliffe, 2008] have kinematically inconsistent boundary conditions [Eilon *et al.*, 2015]. The lithospheric mantle may have been removed from below by some combination of thermal and chemical erosion from upward percolating melts [Holtzman and Kendall, 2010]. Low submoho velocities (Figure 6d) [Jin *et al.*, 2015] and high  $V_P/V_S$  ratios beneath the D'Entrecasteaux Islands [Eilon *et al.*, 2015] indicate the presence of small degrees of upper mantle melts ( $\leq 1\%$ ) or hydration that could contribute to lithospheric degradation. Jin *et al.* [2015] also suggest the potential impact of felsic compositional heterogeneity in explaining the low velocities at lithospheric depth.

The mantle  $V_S$  anomalies inferred from surface waves [Jin *et al.*, 2015] show that the slowest upper mantle and thinnest lithosphere lie directly beneath the D'Entrecasteaux Islands where crust is thinnest and seismicity is most abundant. However, west of Goodenough Island, the low-velocity anomaly continues westward without the southward offset that the surface fault system follows (Figure 10). The pattern in the west can be reconciled with surface faulting if the mantle extension is offset along crustal-scale normal faults. Because earthquakes associated with the Mai'i'u Fault extend to 20–25 km depth along a 30–40° dipping surface (Figure 2, cross-section E-F), at lower crustal depths the fault lies at the center of the mantle rift axis. By contrast, the D'Entrecasteaux fault seismicity does not extend deeper than 10–15 km and flanks both sides of the islands. The Mai'i'u fault system may be one of the few globally where surface faulting can be shown as offset with respect to mantle extension [e.g., Wernicke and Burchfiel, 1982; Davis and Lister, 1988].

## 6.5. Intermediate-Depth Earthquakes and Subducted Material

This study provides the first documentation for intermediate-depth earthquakes (90–120 km deep) close to the axis of the actively extending rift, although these earthquakes are briefly discussed in a companion paper [Eilon *et al.*, 2015]. Such earthquakes worldwide are only found at temperatures less than 700–800°C and are often associated with dehydration reactions in the host rock [e.g., Hacker *et al.*, 2003]. Unfortunately, the

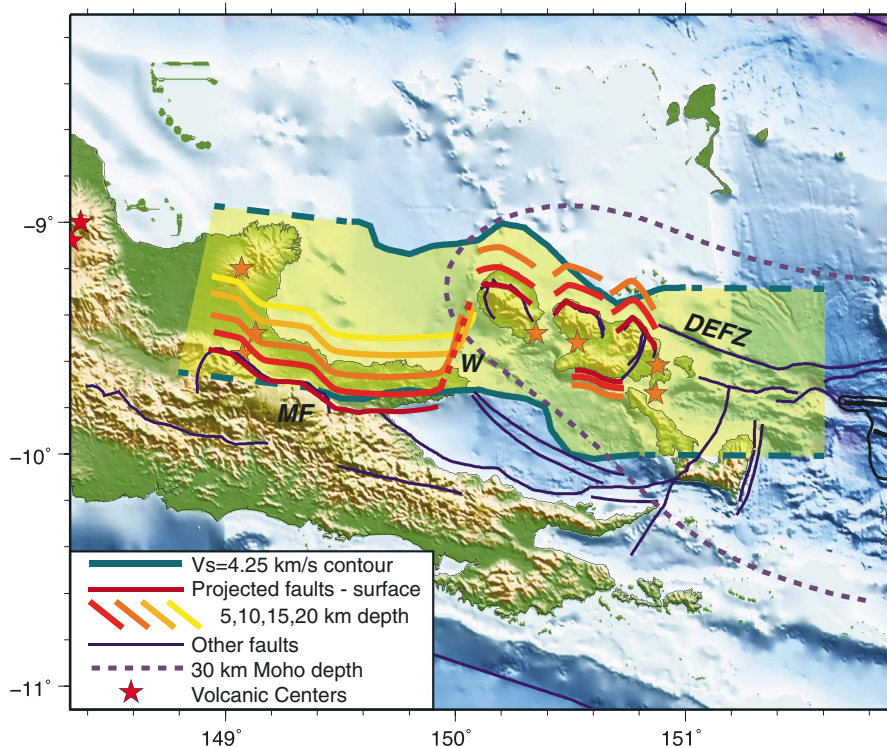


**Figure 10.** Comparison of low-velocity upper mantle anomaly [Jin et al., 2015] to downward projection of surface faults. Yellow field bounded by teal line represents  $V_s \leq 4.25 \text{ km/s}$  at 50 km depth. Purple dashed line shows 30 km Moho depth contour. Red, orange, and yellow lines show major faults projected downward as indicated by seismicity or focal mechanisms, at dips of 30° for north dipping faults and 60° for south dipping faults that are seismically active; geometry of Ward Hunt Strait transfer zone (W) is guessed from seismicity and focal mechanism (Figure 3a). Following the maximum depths of earthquakes, the Mai'i'u Fault is extrapolated to 20 km depth and faults bounding the Goodenough-Fergusson MCCs are extrapolated to 10 km depth. Thick black line east of 151.7°E shows oceanic spreading center, and surrounding black line denotes new oceanic crust. Other symbols and abbreviations are same as Figure 2.

earthquakes are too few to unambiguously describe a dipping Wadati-Benioff zone and there seems to be a clear gap between these earthquakes and crustal seismicity, so the geometry of this zone remains ambiguous. It could represent a remnant slab dipping either north or south, or some other sort of instability; given the broader setting, it is likely that this is a remnant of earlier Tertiary subduction. Teleseismic imaging [Eilon et al., 2015] shows that the earthquakes lie inside an anomalously fast body consistent with such low temperatures, supporting the inference of a cold and possibly damp body just north of the rift axis.

The intermediate-depth earthquakes occur at depths comparable to those that nearby UHP rocks were exhumed at 5–8 Ma so potentially represent evidence of modern processes from the depth region of UHP rocks. The temperatures required for seismogenesis are similar to those recorded by UHP rocks [Baldwin et al., 2008]. While a genetic connection between these earthquakes and exposed UHP rocks is unclear, their existence suggests that conditions for UHP metamorphism may exist today not far from the young UHP localities.

## 7. Conclusions

Continent-like crust of the D'Entrecasteaux-Woodlark rift has undergone and continues to undergo high rates of extension. This extension is manifested in seismicity, in the seismic velocity structure, in crustal motions, in exhumation of high-pressure metamorphic rocks, and in rugged terrain. This study provides a new data set of seismicity and  $V_s$  images of the crust for the region that illustrate how crustal extension exhumes the D'Entrecasteaux-Dayman MCCs.

Seismicity shows a prevalence of active faults bounding the north and south sides of the island MCCs, continuous with the oceanic spreading tip. This deformation is transferred via an oblique transfer fault at the

Ward Hunt Strait to the Mai'iu Fault, which bounds the Dayman Dome. While other secondary fault systems are active, the dominant active deformation likely follows this trend. This modern pattern of deformation follows the maximum depths of seismicity (a proxy for temperature gradient) and depths of the Moho, both of which indicate 30–40% thinning of the crust beneath the D'Entrecasteaux Islands relative to the Papuan Peninsula and Trobriand Platform. Thus, the greatest thinning and greatest seismicity follow the MCCs (including the Dayman Dome) and these structures are likely the site of most of the extension. Roughly 70–100 km of extension must be accounted for at the longitudes of the domes over the last 3.6 Ma, so it seems likely that much of that has taken place in a manner coupled to exhumation of the core complexes.

Shear velocities of the crust and uppermost mantle are generally slower than or similar to continental crust elsewhere. Low crustal velocities ( $V_S < 3.5$  km/s) are observed at all crustal depths beneath the D'Entrecasteaux Islands, while typical continental structure lies beneath the Trobriand Platform and Papuan Peninsula. These observations indicate that the high-density, high-velocity PUB does not make up an observable part of the upper crust here, unlike farther northwest, and so crustal density structure is gravitationally stable. The crust is thinnest beneath the MCCs, so buoyancy due to Moho relief should be negative, and efficient passage of S waves through the MCC crust indicates that it should contain no more than 0.5–8% melt. Seismicity also shows that the MCC-bounding faults continue to operate in response to north-south extension. These observations indicate that MCC exhumation largely results from extensional forces rather than buoyancy.

Deeper structure also provides clues into the origins of the UHP rocks exhumed. Earthquakes at depths of 90–120 km, a few tens of kilometers NW from the D'Entrecasteaux MCCs, indicate that the thermal conditions recorded by the 5–8 Ma UHP terranes (temperatures  $< 750^\circ\text{C}$  at 100 km depth) persist nearby today. While there is no direct structural link between the high-velocity material surrounding the earthquakes and the MCCs, we speculate that they are part of the same subducted, low-temperature body now lying just north of the rift.

## Acknowledgments

This work reflects interactions over a multiyear collaboration funded under the National Science Foundation's Continental Dynamics program, grants EAR-0814236 (Abers) and EAR-0708445 (Gaherty). We acknowledge fruitful discussions and early views of data from many of the collaborators from the CD project and parallel New Zealand Program, including S. Baldwin, R. Buck, S. Ellis, P. Fitzgerald, S. Gordon, B. Hacker, T. Little, P. Mann, T. Plank, P. Ruprecht, and L. Wallace. The text benefitted from careful reviews from S. Ellis and D. Kier. Data collection was supported onshore by the IRIS-PASSCAL Instrument Center and offshore by the Ocean Bottom Seismometer Instrument Program (OBSIP) group at Scripps Institute of Oceanography; we thank E. Aaron, G. Chavez, and M. Fort from those facilities. Fieldwork would not have been possible without additional help from many others, including J. Calkins, H. Davies, P. Irarue, T. Koczynski, E. Nidkambu, J. Oa, and R. Verave and assistance from the PNG Minerals Resources Authority, National Research Institution, UPNG, and the Milne Bay Provincial administration. All original data in this paper are archived and available at the IRIS Data Management Center (<http://ds.iris.edu/ds/>).

## References

- Abers, G. A. (1991), Possible seismogenic shallow-dipping normal faults in the Woodlark-D'Entrecasteaux extensional province, Papua New Guinea, *Geology*, **19**, 1205–1208.
- Abers, G. A. (2001), Evidence for seismogenic normal faults at shallow depths in continental rifts, in *Non-Volcanic Rifting of Continental Margins: A Comparison of Evidence From Land and Sea*, edited by R. C. L. Wilson et al., pp. 305–318, Geol. Soc., London.
- Abers, G. A., and B. R. Hacker (2016), A MATLAB toolbox and Excel workbook for calculating the densities, seismic wave speeds, and major element composition of minerals and rocks at pressure and temperature, *Geochem. Geophys. Geosyst.*, doi:10.1002/2015GC006171.
- Abers, G. A., and S. Roecker (1991), Deep structure of an arc-continent collision: Earthquake relocation and inversion for upper mantle P and S wave velocities beneath Papua New Guinea, *J. Geophys. Res.*, **96**, 6379–6401, doi:10.1029/91JB00145.
- Abers, G. A., C. Z. Mutter, and J. Fang (1997), Shallow dips of normal faults during rapid extension: Earthquakes in the Woodlark-D'Entrecasteaux rift system, Papua New Guinea, *J. Geophys. Res.*, **102**, 15,301–15,317, doi:10.1029/97JB00787.
- Abers, G. A., A. Ferris, M. Craig, H. Davies, A. L. Lerner-Lam, J. C. Mutter, and B. Taylor (2002), Mantle compensation of a region of active metamorphic core complexes, Woodlark Rift, Papua New Guinea, *Nature*, **418**, 862–865.
- Abers, G. A., K. M. Fischer, G. Hirth, D. A. Wiens, T. Plank, B. K. Holtzman, C. McCarthy, and E. Gazel (2014), Reconciling mantle attenuation-temperature relationships from seismology, petrology and laboratory measurements, *Geochem. Geophys. Geosyst.*, **15**, 3521–3542, doi:10.1002/2014GC005444.
- Baldwin, S. L., G. S. Lister, E. J. Hill, D. A. Foster, and I. McDougall (1993), Thermochronologic constraints on the tectonic evolution of active metamorphic core complexes, D'Entrecasteaux Islands, Papua New Guinea, *Tectonics*, **12**, 611–628, doi:10.1029/93TC00235.
- Baldwin, S. L., B. D. Monteleone, L. E. Webb, P. G. Fitzgerald, M. Grove, and E. J. Hill (2004), Pliocene eclogite exhumation at plate tectonic rates in eastern Papua New Guinea, *Nature*, **431**(7006), 263–267, doi:10.1038/nature02846.
- Baldwin, S. L., L. E. Webb, and B. D. Monteleone (2008), Late Miocene coesite-eclogite exhumed in the Woodlark Rift, *Geology*, **36**(9), 735–738, doi:10.1130/g25144a.1.
- Baldwin, S. L., P. G. Fitzgerald, and L. E. Webb (2012), Tectonics of the New Guinea Region, *Ann. Rev. Earth Planet. Sci.*, **40**, 495–520.
- Bodin, T., M. Cambridge, H. Tkalcic, P. Arroucau, K. Gallagher, and N. Rawlinson (2012), Transdimensional inversion of receiver functions and surface wave dispersion, *J. Geophys. Res.*, **117**, B02301, doi:10.1029/2011JB008560.
- Brocher, T. M. (2005), Empirical relations between elastic wavespeeds and density in the Earth's crust, *Bull. Seismol. Soc. Am.*, **95**, 2081–2092.
- Brooks, K., and C. Tegner (2001), Affinity of the Leg 180 dolerites of the Woodlark Basin: Geochemistry and age, in *Proc. ODP Sci. Results*, vol. 180, edited by P. Huchon, B. Taylor, and A. Klaus, pp. 1–18, Ocean Drilling Program.
- Brownlee, S. J., B. R. Hacker, M. Salisbury, G. Seward, T. A. Little, S. L. Baldwin, and G. A. Abers (2011), Predicted velocity and density structure of the exhuming Papua New Guinea ultrahigh-pressure terrane, *J. Geophys. Res.*, **116**, B08206, doi:10.1029/2011JB008195.
- Burchfiel, B. C., K. V. Hodges, and L. H. Royden (1987), Geology of Panamint Valley-Saline Valley Pull-Apart System, California: Palinspastic evidence for low-angle geometry of a Neogene Range-Bounding Fault, *J. Geophys. Res.*, **92**, 10,422–10,426, doi:10.1029/JB092iB10p10422.
- Cairns, E. A., T. A. Little, G. M. Turner, L. M. Wallace, and S. Ellis (2015), Paleomagnetic evidence for vertical-axis rotations of crustal blocks in the Woodlark Rift, SE Papua New Guinea: Miocene to present-day kinematics in one of the world's most rapidly extending plate boundary zones, *Geochem. Geophys. Geosyst.*, **16**, 2058–2081, doi:10.1002/2015GC005788.
- Castagna, J. P., M. L. Batzle, and R. L. Eastwood (1985), Relationships between compressional-wave and shear-wave velocities in clastic silicate rocks, *Geophysics*, **50**, 571–581.
- Christensen, N. I. (1996), Poisson's ratio and crustal seismology, *J. Geophys. Res.*, **101**, 3139–3157, doi:10.1029/95JB03446.

- Christensen, N. I., and W. D. Mooney (1995), Seismic velocity structure and composition of the continental crust; a global view, *J. Geophys. Res.*, **100**, 9761–9788, doi:10.1029/95JB00259.
- Coney, P. J. (1980), Cordilleran metamorphic core complexes: An overview, *Geol. Soc. Am. Mem.*, **153**, 7–31.
- Connolly, J. A. D. (2005), Computation of phase equilibria by linear programming: A tool for geodynamic modeling and its application to subduction zone decarbonation, *Earth Planet. Sci. Lett.*, **236**, 524–541.
- Daczko, N. R., P. Caffi, J. A. Halpin, and P. Mann (2009), Exhumation of the Dayman dome metamorphic core complex, eastern Papua New Guinea, *J. Metamorph. Geol.*, **1**–18.
- Davies, H. L. (1971), Peridotite-gabbro-basalt complex in eastern Papua: An overthrust plate of oceanic mantle and crust, *Bur. Min. Res. Austr. Bull.*, **128**, 48 p.
- Davies, H. L., and A. L. Jaques (1984), Emplacement of ophiolite in Papua New Guinea, *Geol. Soc. London Spec. Pub.*, **13**, 341–349.
- Davies, H. L., and R. G. Warren (1988), Origin of eclogite-bearing, domed, layered metamorphic complexes ("core complexes") in the D'Entrecasteaux Islands, Papua New Guinea, *Tectonics*, **7**, 1–21, doi:10.1029/TC007i001p00001.
- Davies, H. L., E. Honza, D. L. Tiffin, J. Lock, Y. Okuda, J. B. Keene, F. Murakami, and K. Kisimoto (1987), Regional setting and structure of the western Solomon Sea, *Geo-Mar. Lett.*, **7**, 153–160.
- Davis, G. A., and G. S. Lister (1988), Detachment faulting in continental extension; perspectives from the Southwestern U.S. Cordillera, *Geol. Soc. Am. Spec. Pap.*, **218**, 133–159.
- Ebinger, C. J. (1989), Tectonic development of the western branch of the East African rift system, *Geol. Soc. Am. Bull.*, **101**, 885–903.
- Eilon, Z., G. A. Abbers, G. Jin, and J. B. Gaherty (2014), Anisotropy beneath a highly extended continental rift, *Geochem. Geophys. Geosyst.*, **15**, 545–564, doi:10.1002/2013GC005092.
- Eilon, Z., G. A. Abbers, J. B. Gaherty, and G. Jin (2015), Imaging continental breakup using teleseismic body waves: The Woodlark Rift, Papua New Guinea, *Geochem. Geophys. Geosyst.*, **16**, 2529–2548, doi:10.1002/2015GC005835.
- Ekström, G., M. Nettles, and A. M. Dziewonski (2012), The global CMT project 2004–2010: Centroid-moment tensors for 13,017 earthquakes, *Phys. Earth Planet. Int.*, **200**–201, 1–9.
- Ellis, S. M., T. A. Little, L. M. Wallace, B. R. Hacker, and S. J. H. Buiter (2011), Feedback between rifting and diapirism can exhume ultrahigh-pressure rocks, *Earth Planet. Sci. Lett.*, **311**, 427–438.
- Fang, J. (2000), *Styles and Distribution of Continental Extension Derived From the Rift Basins of Eastern Papua New Guinea*, PhD thesis, Columbia Univ., New York.
- Ferris, A., G. A. Abbers, B. Zelt, B. Taylor, and S. Roecker (2006), Crustal structure across the transition from rifting to spreading: The Woodlark rift system of Papua New Guinea, *Geophys. J. Int.*, **166**, 622–634.
- Finlayson, D. M., B. J. Drummond, C. D. M. Collins, and J. B. Connally (1977), Crustal structures in the region of the Papuan Ultramafic Belt, *Phys. Earth Planet. Inter.*, **14**, 13–29.
- Fitz, G., and P. Mann (2013), Tectonic uplift mechanism of the Goodenough and Fergusson Island gneiss domes, eastern Papua New Guinea: Constraints from seismic reflection and well data, *Geochem. Geophys. Geosyst.*, **14**, 3969–3995, doi:10.1002/ggge.20208.
- Forsyth, D. W. (1992), Geophysical constraints on mantle flow and melt generation beneath mid-ocean ridges, in *Mantle Flow and Melt Generation at Mid-Ocean Ridges*, *Geophys. Monogr. Ser.*, vol. 71, edited by J. Phipps-Morgan, D. K. Blackman, and J. M. Sinton, pp. 1–66, AGU, Washington, D. C.
- Gawthorpe, R. L., and J. M. Hurst (1993), Transfer zones in extensional basins: Their structural style and influence on drainage development and stratigraphy, *J. Geol. Soc. Lond.*, **150**, 1137–1152.
- Goodliffe, A. M., B. Taylor, F. Martinez, R. Hey, K. Maeda, and K. Ohno (1997), Synchronous reorientation of the Woodlark Basin spreading center, *Earth Planet. Sci. Lett.*, **146**(1–2), 233–242.
- Gordon, S. M., T. A. Little, B. R. Hacker, S. A. Bowring, M. Korchinski, S. L. Baldwin, and A. R. C. Kylander-Clark (2012), Multi-stage exhumation of young UHP-HP rocks: Timescales of melt crystallization in the D'Entrecasteaux Islands, southeastern Papua New Guinea, *Earth Planet. Sci. Lett.*, **351**–352, 237–246.
- Hacker, B. R., and G. A. Abbers (2004), Subduction Factory 3: An Excel worksheet and macro for calculating the densities, seismic wave speeds, and H<sub>2</sub>O contents of minerals and rocks at pressure and temperature, *Geochem. Geophys. Geosyst.*, **5**, Q01005, doi:10.1029/2003GC000614.
- Hacker, B. R., G. A. Abbers, and S. M. Peacock (2003), Subduction factory 1: Theoretical mineralogy, density, seismic wave speeds, and H<sub>2</sub>O content, *J. Geophys. Res.*, **108**(B1), 2029, doi:10.1029/2001JB001127.
- Hacker, B. R., P. B. Kelemen, and M. D. Behn (2015), Continental lower crust, *Ann. Rev. Earth Planet. Sci.*, **43**, 167–205.
- Hammond, W. C., and E. D. Humphreys (2000), Upper mantle seismic wave velocity: Effects of realistic partial melt geometries, *J. Geophys. Res.*, **105**, 10,975–10,986, doi:10.1029/2000JB900041.
- Hatzfeld, D., V. Karakostas, M. Ziaia, I. Kassaras, E. Papadimitriou, K. Makropoulos, N. Voulgaris, and C. Papaioannou (2000), Microseismicity and fault geometry in the Gulf of Corinth (Greece), *Geophys. J. Int.*, **141**, 438–456.
- Hill, E. J., and S. L. Baldwin (1993), Exhumation of high pressure metamorphic rocks during crustal extension in the D'Entrecasteaux Islands, Papua New Guinea, *J. Metamorph. Geol.*, **11**, 261–277.
- Hill, E. J., S. L. Baldwin, and G. S. Lister (1992), Unroofing of active metamorphic core complexes in the D'Entrecasteaux Islands, Papua New Guinea, *Geology*, **20**, 907–910.
- Holtzman, B. K., and J.-M. Kendall (2010), Organized melt, seismic anisotropy, and plate boundary lubrication, *Geochem. Geophys. Geosyst.*, **11**, Q0AB06, doi:10.1029/2010GC003296.
- International Seismological Centre (2013), On-line bulletin. [Available at <http://www.isc.ac.uk>], Internat'l. Seis. Cent., Thatcham, U. K.
- Jackson, I., and U. H. Faul (2010), Grainsize-sensitive viscoelastic relaxation in olivine: Toward a robust laboratory-based model for seismological application, *Phys. Earth Planet. Int.*, **183**, 151–163.
- Jin, G., and J. B. Gaherty (2015), Surface wave phase-velocity tomography based on multichannel cross-correlation, *Geophys. J. Int.*, **201**, 1383–1398.
- Jin, G., J. B. Gaherty, G. A. Abbers, Y. Kim, Z. Eilon, and R. Buck (2015), Shear velocity structure of the D'Entrecasteaux Islands, Papua New Guinea from Rayleigh wave tomography, *Geochem. Geophys. Geosyst.*, **16**, 3808–3824, doi:10.1002/2015GC005840.
- Karato, S., and H. Jung (1998), Water, partial melting and the origin of the seismic low velocity and high attenuation zone in the upper mantle, *Earth Planet. Sci. Lett.*, **157**, 193–207.
- Kington, J. D., and A. M. Goodliffe (2008), Plate motions and continental extension at the rifting to spreading transition in Woodlark Basin, Papua New Guinea: Can oceanic plate kinematics be extended into continental rifts?, *Tectonophysics*, **458**, 82–95.
- Li, J., G. A. Abbers, Y. Kim, and D. Christensen (2013), Alaska Megathrust 1: Seismicity 43 years after the great 1964 Alaska megathrust earthquake, *J. Geophys. Res. Solid Earth*, **118**, 4861–4871, doi:10.1002/jgrb.50358.

- Ligorria, J. P., and C. J. Ammon (1999), Iterative deconvolution and receiver-function estimation, *Bull. Seismol. Soc. Am.*, **89**, 1395–1400.
- Lin, G. Q., C. H. Thurber, H. Zhang, E. Hauksson, P. M. Shearer, F. Waldhauser, T. M. Brocher, and J. Hardebeck (2010), A California statewide three-dimensional seismic velocity model from both absolute and differential times, *Bull. Seismol. Soc. Am.*, **100**, 225–240.
- Lindley, I. D. (2014), Suckling Dome and the Australian-Woodlark plate boundary in eastern Papua: The geology of the Keveri and Ada'u Valleys, *Aust. J. Earth Sci.*, **61**(8), 1125–1147, doi:10.1080/08120099.2014.965980.
- Little, T. A., S. L. Baldwin, P. G. Fitzgerald, and B. Monteleone (2007), Continental rifting and metamorphic core complex formation ahead of the Woodlark spreading ridge, D'Entrecasteaux Islands, Papua New Guinea, *Tectonics*, **26**, TC1002, doi:10.1029/2005TC001911.
- Little, T. A., B. R. Hacker, S. M. Gordon, S. L. Baldwin, P. G. Fitzgerald, S. Ellis, and M. Korchinski (2011), Diapiric exhumation of the Earth's youngest (UHP) eclogites in the gneiss domes of the D'Entrecasteaux Islands, Papua New Guinea, *Tectonophysics*, **510**, 39–68.
- Lus, W. Y., I. McDougall, and H. L. Davies (2004), Age of the metamorphic sole of the Papuan Ultramafic Belt ophiolite, Papua New Guinea, *Tectonophysics*, **392**, 85–101.
- Maggi, A., J. A. Jackson, D. McKenzie, and K. Priestley (2000), Earthquake focal depths, effective elastic thickness, and the strength of the continental lithosphere, *Geology*, **28**, 495–498.
- Malinverno, A. (2002), Parsimonious Bayesian Markov chain Monte Carlo inversion in a nonlinear geophysical problem, *Geophys. J. Int.*, **151**, 675–688.
- Martinez, F., A. M. Goodliffe, and B. Taylor (2001), Metamorphic core complex formation by density inversion and lower-crust extrusion, *Nature*, **411**(6840), 930–934.
- McCarthy, C., and Y. Takei (2011), Anelasticity and viscosity of partially molten rock analogue: Toward seismic detection of small quantities of melt, *Geophys. Res. Lett.*, **38**, L18306, doi:10.1029/2011GL048776.
- McKenzie, D. P. (1978), Some remarks on the development of sedimentary basins, *Earth Planet. Sci. Lett.*, **40**, 25–32.
- Menke, W., and G. Jin (2015), Waveform fitting of cross spectra to determine phase velocity using Aki's formula, *Bull. Seismol. Soc. Am.*, **105**, 1619–1627.
- Miller, S. R., S. L. Baldwin, and P. G. Fitzgerald (2012), Transient fluvial incision and active surface uplift in the Woodlark Rift of eastern Papua New Guinea, *Lithosphere*, **4**(2), 131–149.
- Mueller, H. J., and H.-J. Massonne (2001), Experimental high pressure investigation of partial melting in natural rocks and their influence on Vp and Vs, *Phys. Chem. Earth A*, **26**, 325–332.
- Mutter, J. C., C. Z. Mutter, and J. Fang (1996), Analogies to oceanic behaviour in the continental breakup of the western Woodlark basin, *Nature*, **380**, 333–336.
- Obrebski, M., G. A. Abers, and A. Foster (2015), Magmatic arc structure around Mt Rainier, WA, from the joint inversion of receiver functions and surface wave dispersion, *Geochem. Geophys. Geosyst.*, **16**, 178–194, doi:10.1002/2014GC005581.
- Ollier, C. D., and C. F. Pain (1980), Active rising surficial gneiss domes in Papua New Guinea, *J. Geol. Soc. Aust.*, **27**, 33–44.
- Pegler, G., S. Das, and J. H. Woodhouse (1995), A seismological study of the eastern New Guinea and the western Solomon Sea regions and its tectonic implications, *Geophys. J. Int.*, **122**, 961–981.
- Petersen, K. D., and W. R. Buck (2015), Eduction, extension, and exhumation of ultrahigh-pressure rocks in metamorphic core complexes due to subduction initiation, *Geochem. Geophys. Geosyst.*, **16**, 2564–2581, doi:10.1002/2015GC005847.
- Pigram, C. J., and H. L. Davies (1987), Terranes and the accretion history of the New Guinea orogen, *BMR J. Aust. Geol. Geophys.*, **10**, 193–211.
- Richter, C. F. (1935), An instrumental earthquake magnitude scale, *Bull. Seismol. Soc. Am.*, **25**(1), 1–32.
- Ruppel, C. (1995), Extensional processes in continental lithosphere, *J. Geophys. Res.*, **100**, 24,187–24,215, doi:10.1029/95JB02955.
- Ruprecht, P., T. A. Plank, G. Jin, and G. A. Abers (2013), Rifting and UHP exhumation in Eastern Papua New Guinea: Temperature and pressure constraints from primitive magmas, 2013 Fall Meeting, AGU, San Francisco, Calif., 9–13 Dec.
- Schmeling, H. (1985), Numerical models on the influence of partial melt on elastic, anelastic and electric properties of rocks. Part I: Elasticity and anelasticity, *Phys. Earth Planet. Int.*, **41**, 34–57.
- Scholz, C. H. (1998), Earthquakes and friction laws, *Nature*, **391**, 37–42.
- Smith, I., and J. Milsom (1984), Late Cenozoic volcanism and extension in eastern Papua, *Geol. Soc. London Spec. Publ.*, **16**(1), 163–171.
- Taylor, B., and P. Huchon (2002), Active continental extension in the western Woodlark Basin: A synthesis of Leg 180 results, in *Proc. ODP, Sci. Results*, vol. 180, edited by P. Huchon, B. Taylor, and A. Klaus, pp. 1–36 , Ocean Drilling Program.
- Taylor, B., A. M. Goodliffe, and F. Martinez (1999), How continents break up: Insights from Papua New Guinea, *J. Geophys. Res.*, **104**, 7497–7512, doi:10.1029/1998JB900115.
- Teyssier, C., and D. L. Whitney (2002), Gneiss domes and orogeny, *Geology*, **30**, 1139–1142.
- Turcotte, D., and G. Schubert (2002), *Geodynamics*, 456 pp., Cambridge Univ. Press, New York.
- Waldhauser, F., and W. L. Ellsworth (2000), A double-difference earthquake location algorithm: Method and application to the northern Hayward Fault, California, *Bull. Seismol. Soc. Am.*, **90**(6), 1353–1368.
- Wallace, L. M., C. Stevens, E. Silver, R. McCaffrey, W. Loratung, S. Hasiata, R. Stanaway, R. Curley, R. Rosa, and J. Taugaloidi (2004), GPS and seismological constraints on active tectonics and arc-continent collision in Papua New Guinea: Implications for mechanics of microplate rotations, *J. Geophys. Res.*, **109**, B05404, doi:10.1029/2003JB002481.
- Wallace, L. M., S. Ellis, T. Little, P. Tregoning, N. Palmer, R. Rosa, R. Stanaway, J. Oa, E. Nidkombu, and J. Kwazi (2014), Continental breakup and UHP rock exhumation in action: GPS results from the Woodlark Rift, Papua New Guinea, *Geochem. Geophys. Geosyst.*, **15**, 4267–4290, doi:10.1002/2014GC005458.
- Webb, L. E., S. L. Baldwin, T. A. Little, and P. G. Fitzgerald (2008), Can microplate rotation drive subduction inversion?, *Geology*, **36**, 823–826.
- Weissel, J., and A. B. Watts (1979), Tectonic evolution of the Coral Sea Basin, *J. Geophys. Res.*, **84**(B9), 4572–4582, doi:10.1029/JB084iB09p04572.
- Weissel, J. K., B. Taylor, and G. D. Karner (1982), The opening of the Woodlark Basin, subduction of the Woodlark spreading system, and the evolution of northern Melanesia since mid-Pliocene time, *Tectonophysics*, **87**, 253–277.
- Wernicke, B., and B. C. Burchfiel (1982), Modes of extensional tectonics, *J. Struct. Geol.*, **4**, 105–115.
- Whitney, D. L., C. Teyssier, P. Rey, and W. R. Buck (2013), Continental and oceanic core complexes, *Geol. Soc. Am. Bull.*, **125**, 273–298.